Chemical Engineering Science 291 (2024) 119905

Contents lists available at ScienceDirect

Chemical Engineering Science

journal homepage: www.elsevier.com/locate/ces

Flow pattern visualization and definition of transition criteria for two-phase flow in Chevron-type corrugated channels

Stefano Passoni [a], Andrea Ferrario [a], Stefano Lorenzi [b], Riccardo Mereu [a,*]

[a] Politecnico di Milano, Department of Energy, via Lambruschini 4a, Milano, 20156, Italy
[b] Politecnico di Milano, Department of Energy, Nuclear Engineering Division, via La Masa 34, Milano, 20156, Italy

ARTICLE INFO

Keywords:
Two-phase flow
Plate heat exchanger
Flow pattern
Visualization
Transition lines

ABSTRACT

This study aims to highlight the factors influencing flow patterns in Plate Heat Exchangers (PHEs) operated with two-phase flows. Our focus is on providing precise definitions of flow regimes and proposing transition boundaries by comparing diverse experimental datasets. To accomplish this, we designed an experimental apparatus for flow visualization through high-speed videos. The videos clarify flow patterns in an upward-flowing air-water mixture within a chevron-type plate heat exchanger. We introduce a new, clearly defined nomenclature and present the results in the form of a flow regime map. Moreover, we reclassify previously documented flow patterns in the literature using our established nomenclature, creating a unified and comparable database of visualization data. Subsequently, we explore semi-theoretical transition criteria and establish new transition boundaries based on the compiled experimental data. These newly determined transition lines are integrated into a comprehensive global flow regime map, advancing our understanding of two-phase flow behavior in PHEs.

1. Introduction

The Plate Heat Exchangers (PHEs) are well-known in the industrial world. They consist of a pack of gasketed or brazed corrugated plates that promote mixing and turbulence in both hot and cold sides thus resulting in enhanced heat transfer. The main advantage of this technology is the high performances related to its compactness. PHEs proved to have a better efficiency respect shell and tubes or other industry-standard heat exchangers. At first, PHEs were mainly gasketed and used only for single phase applications in dairy, food, beverage, mining, meat/poultry, chemical, plastics and wine industries. The use of PHEs in heat, ventilation, air conditioning and refrigeration (HVAC&R) had not been considered until mid-1980s because of the possible leakage from the gaskets. With the increasing importance of the ozone-depletion issues in recent years PHEs have started to be used also for HVAC&R, because they permit to reduce the charge of refrigerants. With the development of Brazed and Semi-Welded PHE the problem of leakage had been solved and specific applications for two-phase flows were developed (Ayub, 2003). In recent years the PHEs have been used also in power generation cycles as both evaporator and condenser. For this kind of applications, the use of gasketed PHEs is limited by the operating conditions, in fact gasketed PHE operating conditions are normally limited to 20 bar and about 150 °C (depending on the materials) (Abu-Khader, 2012). The brazed PHEs can partly overcome this limit since they can be operated up to very high pressure and temperatures. Nowadays, compact plate heat exchangers are actively considered even for application as steam generators in Small Modular nuclear Reactors (SMRs) (Kang et al., 2022) where the use of standard shell and tubes heat exchangers is prohibited by their large volume. The industrial and scientific focus is therefore moving to the study of two-phase flows inside these components.

1.1. State of the knowledge and objectives

The single-phase flow in PHEs has been widely studied and, in Ayub's review (2003), most of the single-phase correlations available in literature are summarized. Moreover, other handbooks report correlation for single phase PHEs design (Thulukkanam, 2000; Martin, 2010).

* Corresponding author.
E-mail addresses: stefano.passoni@polimi.it (S. Passoni), andrea1.ferrario@polimi.it (A. Ferrario), stefano.lorenzi@polimi.it (S. Lorenzi), riccardo.mereu@polimi.it (R. Mereu).

https://doi.org/10.1016/j.ces.2024.119905
Received 12 October 2023; Received in revised form 14 February 2024; Accepted 16 February 2024
Available online 23 February 2024

Most of the studies on two-phase flow in PHEs are focused on specific applications analysis and provide correlations for heat transfer coefficient and friction factor that are limited and lack of generality. This is mainly due to the fact that complexity associated to the two phase flow is also emphasized by the complex geometry of the plates (Ayub et al., 2019; Eldeeb et al., 2016; Amalfi et al., 2016b). While many works focus on the two-phase flows in pipes and an important literature has been published on the topic, for PHEs the two phase fluid dynamics has yet to be studied in deep. In order to comprehend more deeply the performance of PHEs is important to visualize the flow inside the plates and identify the patterns that the two phases assume. Flow patterns regimes are expected to have an impact on both pressure drops and heat transfer coefficient. The published experimental studies that deal with this topic often show scarce agreement one with the other.

The main lack in the literature about flow visualization in PHEs is the absence of systematic studies that evaluate in a comprehensive manner the impact of geometry, flow direction, different fluids and operating conditions on flow patterns. Most of the existing studies deal with a single geometry, a single fluid mixture and a single configuration. The studies that try to compare different geometries, only investigate no more than 3 corrugation angles and corrugation heights, but such even this does not allow to have a complete understanding of such parameters' impact. The flow direction is seldom investigated and studies on inclined channels have never been proposed. Only few studies analyzed the 3 main flow directions (upward, downward and horizontal) and observed a scarce dependence of the flow field on them. The operating conditions are commonly kept as the ambient ones when using an air-water adiabatic mixture, with a deviation in pressure and temperature when using refrigerants accounting for the different saturation conditions. A critical aspect of these studies is that the transitions between flow patterns are generally presented only graphically relying on human observation and hence it becomes difficult to appreciate the impact of the different studies. It becomes therefore important to identify some physics-based correlations to clearly define transition lines as done in Buscher (2019). Moreover, some flow patterns are defined differently depending on the author, the results are generally processed with different data reduction techniques and some fluid dynamic aspects have yet to be entirely clarified.

The aim of this work is therefore to highlight the most important parameters influencing the two-phase flow patterns in PHEs, to describe the flow regimes with a univocal definition and to compare different experimental databases in order to propose new and more general transition lines. To serve this purpose, a novel experimental facility for the flow regime visualization of an air-water mixture flowing upward in chevron-type corrugated channels was developed. The upward flow was taken into account because it is the predominant direction for flow boiling. Particular attention was paid to have a very wide range of operating conditions to identify all the flow regimes observed by other authors and grant a good comparability with such studies. A second highlight of this work is the data-synthesis performed on the different literature databases leading to the grouping of such studies on a single flow regime map with the objective of determining common criteria to identify regimes transitions. The criteria proposed in this work aim to be as general as possible and rely on physical observations. The developed correlation would hence be a starting point for the development of geometry, direction, operating condition and fluid dependent correlations in future works.

The plan of the paper is as following. In Section 2 a literature review reported to introduce the PHEs geometry and to summarize the studies on flow visualization in PHEs. Section 3 reports the details of the experimental facility, operating conditions and instrumentation used to conduct two-phase flow visualization. Moreover the data reduction and the uncertainty analysis are presented in the same section. Section 4 present this study's experimental results. In Section 5, the experimental data from the other studies and the ones from our experiments are plotted on the same flow regime map, compared to check their agreement and new transition lines are proposed. The analysis is then completed by proposing theoretical models for flow patterns prediction and evaluating how well can them represent the experimental databases. Before drawing the conclusions in Section 6, the issue of the applicability of flow pattern maps and flow regime transition lines obtained from adiabatic studies to diabatic ones is briefly discussed and addressed.

2. Literature review

In this section a literature review is proposed to establish a robust framework for our study. The analysis is divided in two subsections. In the first one the geometry of PHEs is introduced and most influencing parameter are highlighted while in the second a short analysis of single-phase flow in PHEs and two-phase visualization are presented and summarized.

2.1. Geometrical characterization of Chevron-type corrugated plates

The most common PHEs corrugation patterns are the Chevron-Type. They are characterized by sinusoidal corrugations that form herringbones pattern on the plate. To form a closed channel, two plates are put in contact with an opposite herringbone direction. This creates a series of contact on the crests of the corrugation. The number of contact points is determined by the corrugation angle. Then plates can be brazed together or gasketed with a direct influence on operating conditions. The brazing process grants the contact points while, in presence of gaskets, all the plates are enclosed in between two thick closing plates (respectively the first and the last) to hold them together. In this case, the frame plates are bolted and the application of the right tightening torque is necessary to grant contact and prevent leakages. The corrugations are periodic along the flow direction except for the inlet and outlet regions that include the portholes. Each plate has in total four portholes (two at the inlet and two at the outlet) placed in the corners. Two portholes per channel are excluded trough gaskets or brazing in order to allow either hot or cold fluid to flow through each channel. Since the portholes are at corners the inlet and outlet regions assume a triangular shape that is not centered on the plate axis affecting the flow distribution. In visualization facilities often the inlet and outlet section are not reproduced but substituted with a two-phase flow distributor/mixer in order to separate the effect of the inlet and the outlet on the flow regime in the corrugated section.

The plates can be described by different geometrical parameters. The first to be considered are the total plate length (L_{tot}) and the plate length excluding the inlet and outlet distribution sections (L_p). These two parameters do not influence the flow field once it is fully developed. Therefore, they have an impact on the pressure drops and exchanged thermal power but not on pressure gradient and heat transfer coefficient. For this reason, visualization in plates of different length (assumed that are observed far enough from entry region) should not be affected by plates planar dimension. Another parameter to be taken into account is the width (B_p) of the plate. If different PHEs are compared using quantities that are expressed per unit area of the channel's section (like superficial velocity, momentum flux or mass flux), the width does not have an impact on flow field as long as the flow is well distributed on the cross section. The corrugations are characterized by the Chevron or corrugation angle (φ) that is defined as relative to the flow direction (some studies use the complementary angle), the corrugation depth (b_p) and the corrugation wavelength (λ) that is defined as the distance between the crests measured in the direction perpendicular to the crests themselves. All these parameters are summarized in Fig. 1.

The plates with corrugation angles of less than 45° are called "soft plates" while if the angle is higher than 45° are called "hard plates". The difference between the two types is the trade-off between heat transfer efficiency and pressure drops in the channels. Soft plates have lower pressure difference but also a lower heat transfer capability with respect to hard plates. Generally speaking, all the parameters related to

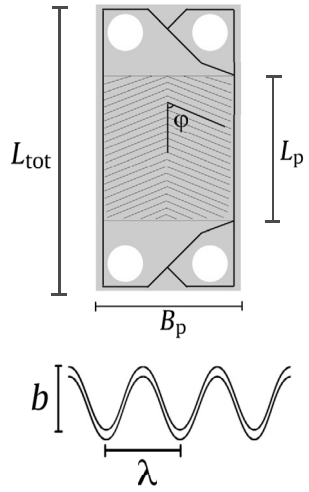

Fig. 1. Chevron Type plate with the main geometrical parameters indicated.

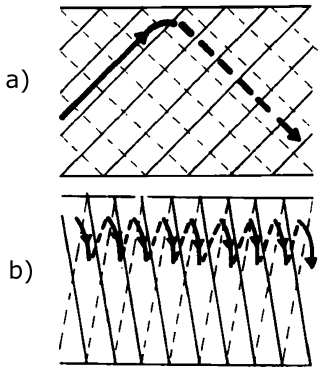

Fig. 2. Single Phase flow paths observed by Focke and Knibbe (1986) a) Crossing Flow b) Wavy Longitudinal Flow.

the corrugations affect the flow field. The higher is the corrugation angle, the higher is its impact on the fluid direction. A corrugation or wave number can be defined as a proxy of how much the corrugation is accentuated:

$$\chi = \frac{\pi b_p}{\lambda} \tag{1}$$

The area enlargement factor Φ, instead, is the ratio between the corrugated surface and the surface of a flat plate with same length and width. Enlargement factor can be obtained parameterizing the corrugation as a sinusoidal function and computing the ratio between the line integral and the wavelength (integration from 0 to $\frac{\pi}{2}$) which yields eq. (2). Martin (2010) suggests an expression of Φ given in equation (3) that can be obtained by using the Simpson's rule to compute the integral (2):

$$\Phi = \frac{2}{\pi}\int_0^{\frac{\pi}{2}} \sqrt{1+\chi^2 cos^2(t)}dt \tag{2}$$

$$\Phi = \frac{1}{6}\left(1+\sqrt{1+\chi^2}+4\sqrt{1+\frac{\chi^2}{2}}\right) \tag{3}$$

The enlargement factor can be used to compute the hydraulic diameter D_h assuming that the average channel section is equal to the corrugation depth according to the following definition:

$$D_h = \lim_{b_p \to 0} \frac{4 b_p B_p}{2(\Phi B_p + b_p)} = \frac{2 b_p}{\Phi} \tag{4}$$

2.2. Previous studies on flow visualization in PHEs

In order to understand two-phase flow characteristics, it is necessary to describe how a single-phase fluid flows into a PHE. Focke and Knibbe (1986) visualized the streaklines using a pH indicator and recognized two different directions (Fig. 2): crossing flow and wavy longitudinal flow. The crossing flow was observed for soft plates with corrugation angles of 30°, the fluid flowed along the corrugations' valleys only changing its direction at the boundary. Tribbe and Müller-Steinhagen (2001b) traced particles in single phase flow and recognized that also the central spine of the plate acts like a boundary. The wavy longitudinal flow was observed by Focke and Knibbe (1986) for hard plates with 80° of corrugation angles, the preferred direction of the fluid particles was longitudinal but the crests forced an helical path around the contact points. Martin (2010) stated that the two directions occurs at the same time but the increase or decrease of the angle cause one or the other to become predominant. Tribbe and Müller-Steinhagen (2001b) recognized both the two directions in their visualizations on 60° Plates.

There are many studies that focus on two-phase fluid dynamics in PHEs with the aim of obtaining useful correlations for pressure drops and heat transfer coefficients. The interested reader can refer to the reviews of Ayub et al. (2019), Amalfi et al. (2016a), Tao et al. (2018) and Eldeeb et al. (2016). On the other hand, only a few studies visualized and investigated flow patterns and their influence on PHEs performance. For this reason in present work it has been decided to review such studies and to contribute in deepening the knowledge with own experimental investigation.

The first study on PHEs two-phase flow was led by Gradeck and Lebouché (2000). Horizontal PHEs with bidimensional and three dimensional corrugation geometries were investigated. The investigated range was limited to low gas superficial velocities (lower than 0.15 m/s) and only a transition from a bubbly flow and a stratified flow could be recognized. The wall shear stress measurements allowed to associate phase distribution to fluid dynamic phenomena.

Tribbe and Müller-Steinhagen (2001a,b) published a two part study on two-phase flow in a PHE operated in upward and downward adiabatic configuration. The first part is focused on pressure drop measurement and the second on analyzing the results with the separated flow approach and visualize flow patterns in air/water systems. The direction of the flow impacted the regimes only for high mass flow rates. Fluid viscosity effect was analyzed using an aqueous solution of carboxymethylcellulose and it was observed that pressure drops increase noticeably at low quality but tend to converge to air/water for high quality. The separated flow analysis permitted to develop a unique correlation for both hard and mixed plates in all conditions. In soft plates instead a dependence on geometry and liquid viscosity was observed. Five different flow pattern were identified: regular bubbly, irregular bubbly, churn flow, film flow and partial film flow. The flow regimes were summarized in flow maps and it was observed that soft and mixed plates exhibit same transition lines while the hard plates had a larger churn region.

Vlasogiannis et al. (2002) conducted experiments to visualize multiphase flow and measure heat transfer in a real industrial PHE operated with downward air/water mixture. Three main regimes named A, B and C and two transition regimes AB and BA were observed. In regime A phases were observed to flow separately, in regime B the gas phase was dispersed into liquid phase and regime C was intermittent. The regimes were reported on a flow map. Heat transfer measurements were carried out for both single and two phase flow. A correlation was proposed for single phase flow heat transfer coefficient. The two-phase flow heat transfer were analyzed only qualitatively, an increase of heat transfer was observed for higher gas qualities.

Shiomi et al. (2004) visualized air/water two-phase flow in PHEs mounted horizontally and vertically. Plates with 30° and 60° corrugation angles were used also in mixed configuration. Flow patterns were recognized via visual observation and pressure drops were also

measured during testing. In horizontal flow only two patterns were observed: dispersed bubbly flow and stratified flow. In vertical flow only dispersed flow was observed as well as strong maldistribution for low flow rates. The bubble dimension was observed to decrease with an increase of liquid velocity. Pressure drops in single phase increased with corrugation angle. Two-phase multipliers for pressure drops were plotted using Lockhart-Martinelli parameter and showed a good agreement with the model proposed by Chisholm (1967).

Asano et al. (2004) focused on flow visualization in upward PHEs using neutron radiography and image processing methods. Tests were operated in adiabatic conditions using air and water or in boiling condition using R141b. Void fraction was obtained by processing images. It was recognized that the homogeneous flux does not well represent the void fraction. Pressure drops were measured and a correlation was proposed using the Lockhart-Martinelli approach. In a following paper (Asano et al., 2005) the author analyzed both upflow and downflow configuration. Agreement on void fraction was found for upward and downward configuration. Multichannel configuration was analyzed and the distribution of void fraction reported. Neutron radiography did not permit to obtain instantaneous images but only averaged results, hence flow patterns characteristics could not be recognized.

Nilpueng and Wongwises (2010) studied upward and downward two-phase flow in unsymmetrical plates, focusing on visualization and pressure drops evaluation. The plates were characterized by different angles in the two halves of the channel: 80° and 35°. With the upward-flow setup three patterns were observed: bubbly flow, bubble recirculation flow and annular-liquid bridge flow. With the downward setup, three patterns were observed: Slug flow, Annular-liquid bridge and Annular-liquid bridge/air-alone flow. Flow maps were proposed. Pressure drops were measured for water single-phase flow and a correlation was obtained. For two-phase measurements, instead, a correlation for two-phase multiplier as function of Lockhart-Martinelli parameter was presented.

Solotych et al. (2016) measured heat transfer distribution and pressure drops in PHEs during flow boiling in upflow configuration and also carried out adiabatic flow visualization. In the diabatic configuration HFE7100 was used as fluid and the heat flux was imposed. Pressure drops were measured in single and two-phase conditions and compared with literature. Local temperature was measured with an IR camera and local heat transfer coefficient was derived. At high mass and heat fluxes dryout was observed to occur, reducing the heat transfer coefficient. Also heat transfer coefficient measurements were compared with literature. The adiabatic test were carried out in order to identify flow patterns.

Grabenstein et al. (2017) studied two-phase downward flow in PHEs using two different experimental setups, one for air/water flow and saturated R365mfc, the other for condensing R134a. Flow patterns were visualized and pressured drop measured. The Chevron angle impact was evaluated analyzing plates with 30° and 60° angles. The results were presented on a momentum flux map. Flow patterns according to Tribbe nomenclature were identified and capacitance measurements were adopted to identify intermittent flows. Pressure drop was correlated with an homogeneous and a separated flow model, an interpolation between the two models was suggested.

Jin and Hrnjak (2017) visualized and measured heat transfer in a 3 channel PHE. Visualization was conducted in an upward adiabatic configuration using R245fa as operating fluid. The commercial inlet region was observed to cause a maldistribution of the flow that in some conditions also caused flooding. Flooding was recognized to occur when the flow is wavy or stratified in the inlet tube. On the other hand high mass quality proved to stabilize the flow avoiding flooding. Coupled measurement of heat transfer and visualization in boiling condition were also presented. Variations in heat transfer coefficient corresponded to the changes in visual flow patterns. The onset of nucleate boiling and the dry-out were recognized, in the lower corner opposite to the inlet a very strong nucleation was observed and a fast transition occurred.

Buscher published two studies (Buscher, 2019, 2021) regarding flow visualization in PHEs. In the first study, flow pattern visualization was performed and in the second pressure drop and maldistribution were investigated. The visualizations were obtained in upward, downward and horizontal configuration. The observed flow patterns were: regular bubbly flow, irregular bubbly flow, Taylor-like bubbly flow, heterogeneous flow, partial film flow and film flow. Moreover, a stagnant flow was observed only in downward operations for low liquid and gas superficial velocities. A characterization of flow patterns based on the film ratio was proposed. Transitions criteria were developed and flow maps were built. The pressure drops were measured for both well and maldistributed flows. Correlations for Darcy friction factor in single phase were obtained. An homogeneous model was deemed effective for evaluating two phase pressure drops with low void fraction. A new correlation valid for both well and maldistributed flows was presented for high void fraction cases, the impact of maldistribution consisted in a reduction of the void fraction for which this other model should be applied. The author proposed the use of an hydrostatic correction factor to account for differences in void fraction distribution among the three main flow directions. The horizontal one was taken as benchmark to evaluate the effect of the gravitational component of pressure drop on the two-phase friction factor.

The reviewed studies are summarized in Table 1 and 2. In the first table for each study are also reported the geometrical characteristics of the analyzed plates. In the second table instead are reported the operating conditions, the working fluids, the flow direction and the investigated range.

3. Methods

3.1. Experimental apparatus

In order to complete the analysis to be presented later in this work and to define a unique nomenclature of observed flow patterns, the authors conducted some experimental work to visualize two-phase flow in a Chevron-type corrugated channel. In Fig. 3–5 the plant scheme of the employed experimental facility is depicted as well as the original steel plate. It consists in a closed-loop water circuit and an open loop compressed air circuit. The water is pumped into the circuit from an atmospheric tank and flow rate measured through three rotameters covering different ranges and regulated using needle valves at their outlet. The compressed air was supplied by centralized compressed air line and its pressure reduced trough a pressure-regulation valve. The air flow rate was measured using 3 different range rotameters in parallel with a bypass used for start up operations. The flow rate was regulated with a single valve downstream of the rotameters. A special mixing section was developed: both air and water lines were separated in two branches and fed to two distributors. Each one divided the flow in 4 smaller-diameter lines and mixing was obtained trough T-junctions. Regulation valves were located at the outlet of air distributors in order to avoid unequal flowrate between the tubes. The mixed fluids flow into a plenum containing a perforated plate to homogenize the flow and then enters the corrugated plate channel. At the outlet of the channel, the mixture flows into a collector and then is sent to the feeding tank where air is vented spontaneously. The water rotameters used had a range of 100, 400 and 2500 $\frac{l}{h}$ with an uncertainties of 3% of fullscale range while the air ones had a range of 190, 800 and 4000 $\frac{l}{h}$ with the same accuracy.

The visualization section consisted in two replica transparent plates obtained by pouring resin into a silicone mold created from original plates of a CPHE. The plates were created using an epoxy resin (EpoxAcast^{TM} 690) that offers both excellent transparency and good mechanical properties. The resin properties are reported in Table 3. The plates presented a chevron pattern with corrugation angles of 63°. All the plates geometrical characteristics are summarized in Table 4.

In order to visualize the flow pattern, the corrugated channel was lighted with a flicker-free, DC LED panel and high frame rate videos

Table 1
Plate geometry details of the reviewed studies.

Author	Corrugation Angle (φ) [deg]	Corrugation Depth (bp) [mm]	Corrugation Wavelength (λ) [mm]	Plate Width (Bp) [mm]	Corrugation Length (Lp) [mm]	Wave Number (χ) [-]	Enlargement Factor (Φ) [-]	Hydraulic Diameter (Dh) [mm]
Gradeck and Lebouché (2000)	90 and 60	20	65	not reported	not reported	0.96	1.21	33
Tribbe and Müller-Steinhagen (2001a,b)	30, 60 and 30/60	3 or 2[a]	not reported	210	640	not reported	not reported	not reported
Vlasogiannis et al. (2002)	60	2.4	10	123	430	0.75	1.13	4.24b
Shiomi et al. (2004)	30, 60 and 30/60	3.5	9	162	435	1.22	1.31	5.34
Asano et al. (2004, 2005)	70 and 60	1.2, 2.5 and 1.4	8 and 6.4	145, 150 and 76	180, 200 and 149	0.98, 0.47 and 0.68	1.21, 1.05 and 1.11	4.1, 2.3 and 2.5
Nilpueng and Wongwises (2010)	35/80	2.5	not reported	124	715	not reported	not reported	not reported
Solotych et al. (2016)	60 and 65	2 and 1	5.7 and 3.7	50	99	1.1 and 0.84	1.26 and 1.16	3.2 and 1.7
Grabenstein et al. (2017)	27 and 63	3	11.4	388	408	0.85	1.16	5.2
Jin and Hrnjak (2017)	60	2.2	10	210	425	0.69	1.11	3.96
Buscher (2019, 2021)	75	2.4	9	278.2	326.1	0.84	1.16	4.14

[a] Only for pressure drop measurement.

Table 2
Operating conditions of the reviewed studies.

Author	Operating Pressure [kPa]	Operating Temperature [°C]	Working Fluid	Flow Direction	$V_{s,G}$ range [m/s]	$V_{s,L}$ range [m/s]	Mass Flux range (G) [kg/m^{2}s]
Gradeck and Lebouché (2000)	not reported[a]	not reported	Electrolytic Solution/Nitrogen	Horizontal	not reported	not reported	not reported
Tribbe and Müller-Steinhagen (2001a,b)	Not reported[b a]	25	Air/Water, Air/CMC$_{(aq)}$[c]	Downward, Upward[c]	1.8 - 55	0.04 - 0.6	60 - 600
Vlasogiannis et al. (2002)	Not reported[a]	25	Air/Water	Downward	0.3 - 10	0.01 - 0.25	10 - 260
Shiomi et al. (2004)	Not reported[a]	Not reported	Air/Water	Upward, Horizontal	0.14 - 1.2	0.01 - 0.56	10 - 560
Asano et al. (2004, 2005)	Not reported[b] (Water) 180 (R141b)	Not reported (Water) 50 (R141b)	Air/Water, R141b	Upward, Downward	0.8 - 8	0.02 - 0.04	20 - 50
Nilpueng and Wongwises (2010)	Not reported[a]	Not reported[b]	Air/Water	Downward Upward	0.06 - 4	0.03 - 0.3	30 - 300
Solotych et al. (2016)	100	61	HFE7100	Upward	not reported	not reported	25 - 100
Grabenstein et al. (2017)	87 (R365mfc), Not reported (H$_2$O[a], R134a)	20	Air/Water, R365mfc, R134a[c]	Downward	0.7 - 15	0.03 - 0.7	30 - 720
Jin and Hrnjak (2017)	105	15.8	R245fa	Upward	0.33 - 1.63	0.0015 - 0.03	10 - 50
Buscher (2019, 2021)	110 to 220	19 to 29	Air/Water	Downward, Upward, Horizontal	0.007 - 30	0.04 - 0.4	40 - 440

[a] Tank at atmospheric conditions.
[b] Measured but not reported.
[c] Only for pressure drop measurement.

were taken using a Phantom Miro C110 high speed camera, sampling at 1900 frames per second with a resolution of 1280x480 pixels and an exposure time of 40 μs.

The facility was operated in upward configuration, the operating temperature of air was always comprised between 18 °C and 21.5 °C, while the water temperature was kept between 23 °C and 26 °C due to pump heating effect. The operating gauge pressure of the plate was measured using manometers and during operations, it varied between 3000 Pa and 50000 Pa. Because of the high operating pressures measured, clamps were applied in the lower part of the visualization win-

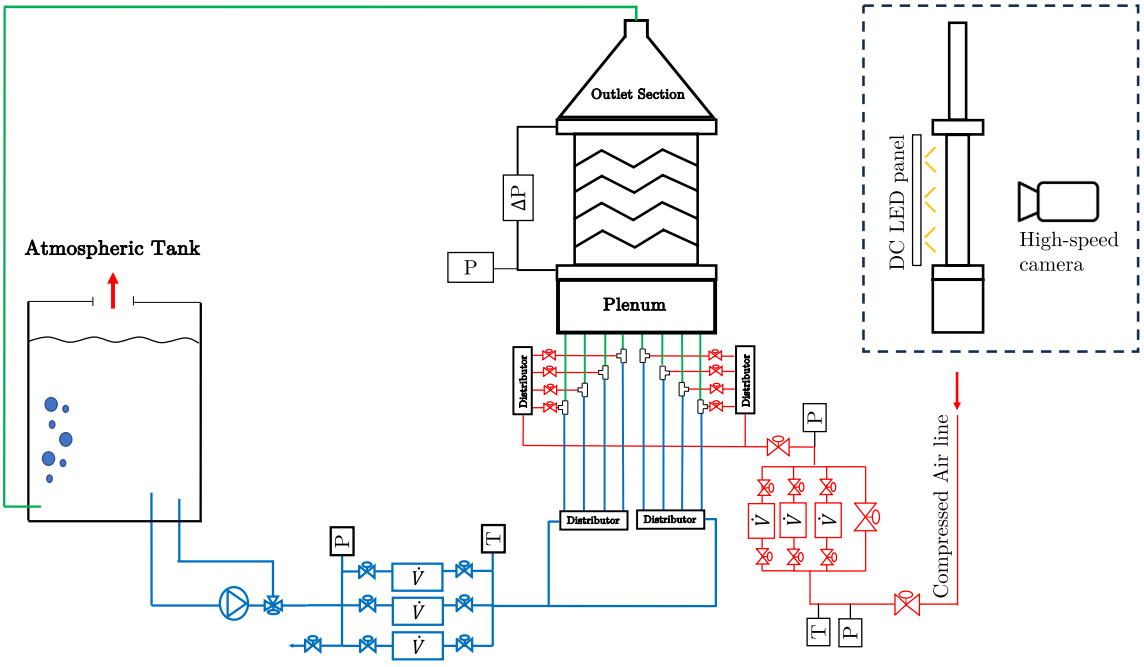

Fig. 3. Schematic of the loop adopted for the experiments.

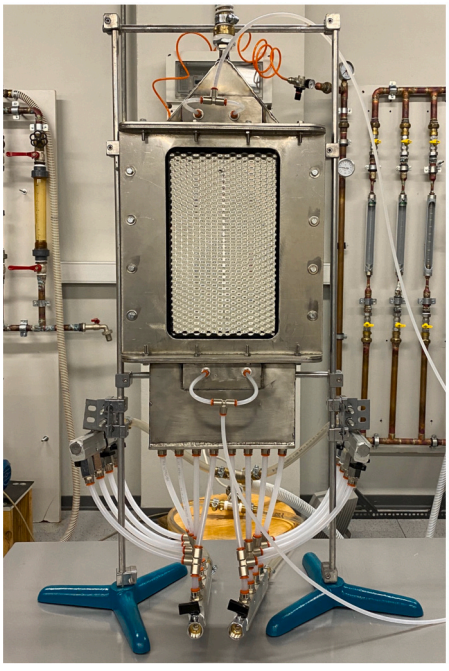

Fig. 4. The experimental facility used for visualization.

Fig. 5. Section of the original plate with the Chevron pattern adopted in the experiments.

dow to reduce the deformation of the plates and therefore avoid the loss of contact points. A preliminary analysis was conducted to identify the optimal conditions for tightening plates and clamps. The goal was to prevent plate deformation during operations and to verify the contact between corrugation crests.

3.2. Data reduction

The results of this study are presented in terms of superficial velocity of both phases. This choice was done because the superficial velocity, being a volumetric flux, is specific to the frontal area and most of studies adopt the same approach. It could be pointed out that this approach is not fluid independent, but since almost all studies presenting flow maps adopt air and water as operating fluids, our study is fully comparable. On the other hand Grabenstein et al. (2017) used a different approach reporting the flow maps based on the momentum flux stating that results of air/water and R365mfc are more consistent on such a basis. Since such method was applied only on 2 different fluids, its validity could not be verified. Future works on different fluid impact should consider it and eventually validate it.

The phase superficial velocities were not directly measured but derived from flow rate measurements. The gas volumetric flow rates read by rotameters was converted to real operating conditions accounting for difference in temperature and operating pressure from calibration condition. To this end the following compensation equation was used:

Table 3
EpoxAcast™ 690 Properties.

Handling Properties		
Mix Ratio By Weight	100:30	(Resin:Hardener)
Mixed Viscosity	0.28	$[Pa \cdot s]$
Density	1107	$[kg/m^3]$
Physical Properties		
Shore D Hardness	80	
Ultimate Tensile Strength	45.7	$[N/mm^2]$
Tensile Modulus	3943	$[N/mm^2]$
Tensile Elongation	1.8	
Flexural Strength	75.7	$[N/mm^2]$
Flexural Modulus	2826.9	$[N/mm^2]$
Compressive Strength	66.3	$[N/mm^2]$
Compressive Modulus	629.5	$[N/mm^2]$
Shrinkage	0.002	$[mm/mm]$
Heat Deflection Temp.	46	$[°C]$
Index of Refraction	1.565	at 20 °C

Table 4
Geometrical parameters of present study's plates.

Corrugation Angle	φ	63°
Corrugation Depth	b_p	2.5 mm
Corrugation Wavelength	λ	9 mm
Plate Width	B_p	18.2 cm
Plate/Corrugation Length	L_p	32 cm
Hydraulic Diameter	D_h	4.3 mm
Enlargement Factor	Φ	1.1712
Frontal Area	A_f	455 mm^2

$$Q = \frac{\left(P_{rot} P_{cal}\right)^{0.5}}{P_{PHE}} \left(\frac{T_{PHE}}{T_{cal}}\right)^{0.5} Q_{read} \tag{5}$$

In this equation subscript *rot* stands for rotameter, *cal* for calibration and PHE for plate heat exchanger. It is worth noticing that PHE pressure is not constant along the plate, hence the average pressure was considered. Some of the other studies refer their results to standard conditions, fixing such value to 1 atm. The obtained flow rate was then divided by plates' frontal area to obtain the superficial velocities:

$$v_{s,i} = \frac{Q_i}{A_f} \tag{6}$$

Considering the corrugation profile as a sinusoidal function, the frontal area can be computed as the double of the semi-channel area as following:

$$A_f = 2 \int_0^m \frac{b_p}{2} \left(1 + \sin\left(\frac{2\pi x}{m}\right)\right) dx \tag{7}$$

$$m = \frac{\lambda}{\cos\varphi} \tag{8}$$

This formula can be approximated by considering a constant and a finite number of wavelengths across the plates' width. As a result, the equation (7) becomes:

$$A_f = b_p B_p \tag{9}$$

3.3. Uncertainty analysis

The uncertainty analysis was carried out following the directives of the Joint Committee for Guides in Metrology (JCGM, 2008). The instrumentation uncertainty was provided by the producer according to the calibration, in Table 5 the measurement uncertainty is reported. The general expression for expanded uncertainty of a generic function f depending by n variables is:

Table 5
Instrumentation uncertainty.

Instrument	Absolute Uncertainty
Rotameters:	
ASA P13 250-2500 l/h	75 l/h
ASA P13 40-400 l/h	12 l/h
ASA P13 10-100 l/h	3 l/h
ASA E 400-4000 nl/h	80 nl/h
ASA E 85-850 nl/h	17 nl/h
ASA E 0-190 nl/h	3.8 nl/h
Manometer located:	
Upstream Air Manometer	5000 Pa
Plenum Pressure Tap	5000 Pa
Outlet Pressure Tap	5000 Pa
Thermometer located:	
Downstream Water Rotameters	0.5 °C
Upstream Water Rotameters	0.5 °C
Geometry Measurements:	
Corrugation Depth	0.05 mm
Plate Width	0.5 mm

$$e_f = \sqrt{\sum_{n=1}^{N} \left(\frac{\partial f}{\partial x_n} e_{x_n}\right)^2} \tag{10}$$

The expanded uncertainty of superficial velocities can be computed combining the uncertainties due to the flow rate and to the frontal area since these two parameters depend by different variables:

$$e_{v_{s,i}} = \sqrt{\left(\frac{\partial v_{s,i}}{\partial A_f} e_{A_f}\right)^2 + \left(\frac{\partial v_{s,i}}{\partial Q_i} e_{Q_i}\right)^2}$$
$$= v_{s,i} \sqrt{\left(\frac{e_{A_f}}{A_f}\right)^2 + \left(\frac{e_{Q_i}}{Q_i}\right)^2} \tag{11}$$

The flow rate uncertainty has been assumed to be the rotameter uncertainty for liquid phase, while for the gas phase it was evaluated as the combined uncertainty of Eq. (5). In particular applying Eq. (10) to Eq. (5) and evaluating the derivatives it can be obtained the following equation:

$$e_{Q_g} = Q_g \sqrt{\left(\frac{e_{Q_{read,g}}}{Q_{read,g}}\right)^2 + \left(0.5 \frac{e_{P_{man}}}{P_{man}}\right)^2 + \left(0.5 \frac{e_{T_{pl}}}{T_{pl}}\right)^2 + \left(\frac{e_{P_{pl}}}{P_{pl}}\right)^2} \tag{12}$$

Where $Q_{read,g}$, P_{man}, T_{pl} and P_{pl} are respectively the read flow rate at the rotameter, the measured pressure at the rotameter, the measured temperature at the plate and the measured pressure at the plate. The uncertainty of the mean plate pressure has to be corrected considering the averring procedure as following:

$$P_{mean} = \frac{P_{in} + P_{out}}{2} \tag{13}$$

$$\frac{\partial P_{mean}}{\partial P_{in}} = \frac{\partial P_{mean}}{\partial P_{out}} = \frac{1}{2} \tag{14}$$

$$e_{P_{mean}} = \sqrt{\left(\frac{e_{P_{in}}}{2}\right)^2 + \left(\frac{e_{P_{out}}}{2}\right)^2} = \left[e_{P_{in}} = e_{P_{out}}\right] = \frac{e_P}{\sqrt{2}} \tag{15}$$

The uncertainty associated to the geometry was computed considering both the effect of the measurement and the approximation of finite number of wavelengths. The combined uncertainty was computed applying Eq. (10) to Eq. (9) and obtaining:

$$e_{A_f} = \sqrt{\left(b_p e_{B_p}\right)^2 + \left(B_p e_{b_p}\right)^2 + \left(e_{approx}\right)^2} \tag{16}$$

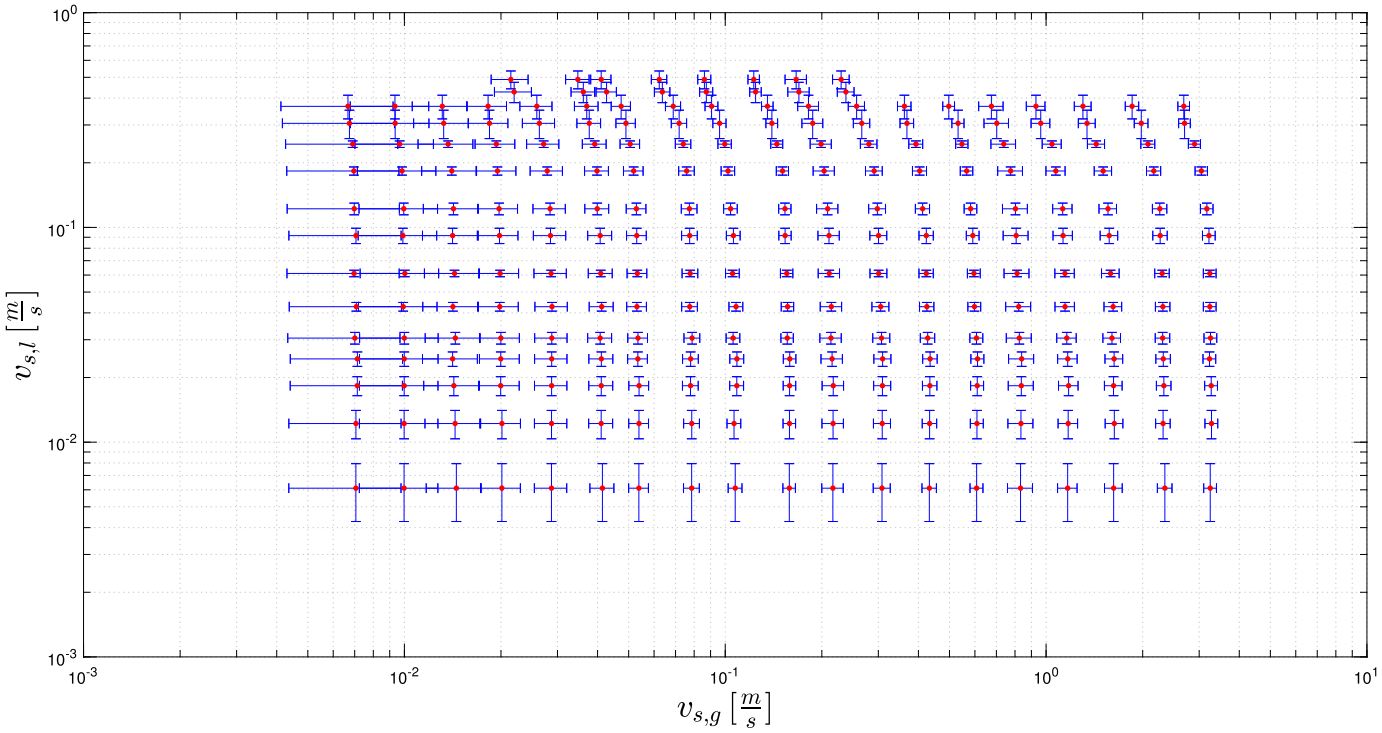

Fig. 6. Test matrix with associated uncertainty as errorbars.

The uncertainty due to the constant frontal area approximation was computed as the maximum difference between the integral function of the area and the approximation without specifying the plate width:

$$e_{approx} = max\left[2\int_0^x \frac{bp}{2}\left(1+\sin\left(\frac{2\pi x}{m}\right)\right)dx - b_p x\right]$$
$$= max\left[-\frac{mb_p}{2\pi}cos\left(\frac{2\pi x}{m}\right)\right] \quad (17)$$

$$e_{approx} = \frac{mb_p}{2\pi} = \frac{\lambda b_p}{2\pi\cos\varphi} \quad (18)$$

The computed uncertainty is reported as error bars on the test matrix hereby reported in Fig. 6. The values of minimum, maximum and average uncertainty on the gas superficial velocity are 4.1%, 38.2% and 10.1% respectively while for the liquid these values become 3.5%, 30.0% and 9.8%. The most impactful uncertainty component is the one on the flow rate which maximum at the lowest superficial velocities.

4. Results

The observations were conducted for a liquid superficial velocity ranging between 0.006 and 0.5 m/s and a gas superficial velocity in between 0.006 and 3.3 m/s. The high speed camera allowed to record videos and classify each point on the basis of its flow features. In this section the flow patterns are described analyzed and then represented on a flow map.

4.1. Flow patterns definition

The nomenclature used to identify the patterns observed during the campaign was the same adopted by Buscher (2019) but with some minor changes to avoid ambiguity. The observed flow patterns were named: Coarse Bubbly Flow, Fine Bubbly Flow, Taylor-like Bubbly Flow, Heterogeneous Bubbly Flow, Partial Film Flow, Film Flow and Unstable Flow. The changes made to Buscher's nomenclature consist in substituting the Regular and Irregular Bubbly Flow with Fine and Coarse Bubbly Flow, because the definition of Irregular Bubbly Flow is ambiguous as it is used with different meaning in some studies like Tribbe and Müller-Steinhagen (2001a) and Grabenstein et al. (2017). Moreover, Unstable flow regime was also defined to identify the conditions for which an intermittent behavior was observed. All the observed two-phase flow patterns can be furthermore categorized in 4 main macro patterns: bubbly flows, film flows, transition flows and intermittent flows. In the following paragraphs the main features of each flow pattern will be described.

4.1.1. Bubbly flows

The bubbly flow is a flow pattern characterized by the liquid phase flowing mixed with gas bubbles. A distinction can be made between fine bubbly flow and coarse bubbly flow depending on the bubble dimension. The most important mechanisms that govern bubble dimension in a two-phase flow are bubbles coalescence and bubbles breakage. The coalescence is determined by the interaction of two bubbles that come in contact and merge. The breakage instead, is due to the turbulence or shear stress that deform the bubbles interface breaking them. The distinction between fine and coarse is determined by the predominance of coalescence over the breakage mechanism in the coarse bubbly flow. In fine bubbly flow, the bubbles are observed to be roundish and to flow in both crossing flow and wavy longitudinal directions as observed in single phase flow by Focke and Knibbe (1986), moreover re-circulation of bubbles is observed behind contact points. The recirculating bubbles are slightly larger. In Coarse Bubbly flow, only the wavy longitudinal direction is observed with the bubbles assuming a zig-zag path around the contact points. The breakage occurs only at the contact points between the two plates. Bubbles hitting these points are deformed and broken into smaller ones as can be observed in Fig. 7. The shape of coarse bubbles tends to be more elliptical than spherical. In Fig. 8a and 8b clear images of a fine and coarse bubbly flow are reported.

4.1.2. Film flow

The film flow is the PHEs' counterpart of the tubes' annular flow, it consists in a thin liquid film flowing next to the wall while the gas occupies the core of the channel. Because of the plates' geometry, at the

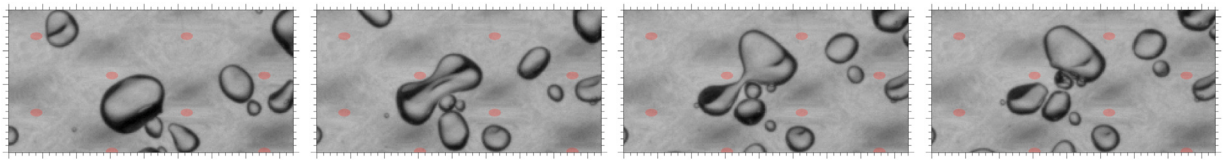

(a) $t = 0\,[s]$ (b) $t = 14.2\,[ms]$ (c) $t = 24.7\,[ms]$ (d) $t = 27.4\,[ms]$

Fig. 7. An example of bubble breakage at contact points. Pictures from experiments. Red dots represent contact points. Minor axis ticks in millimetres [*mm*].

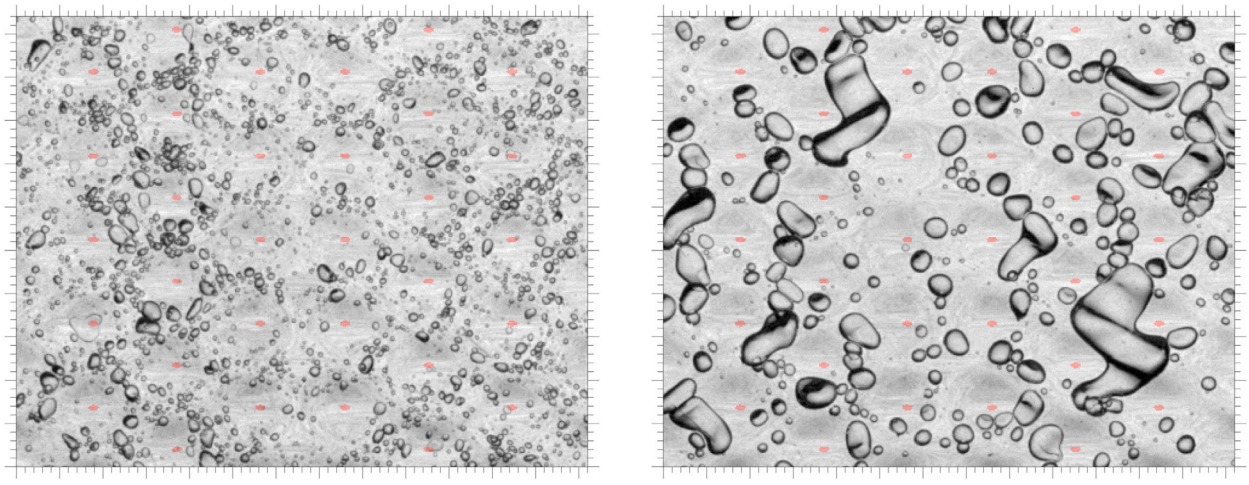

(a) (b)

Fig. 8. Example of fine (a) and coarse (b) bubbly flow. Pictures from experiments. Red dots represent contact points. Minor axis ticks in millimetres [*mm*].

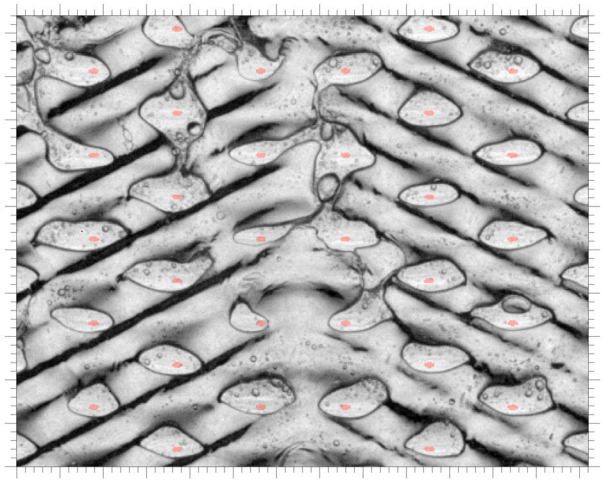

Fig. 9. Film flow, the lighter regions are the liquid pockets at contact points. Picture from experiments. Red dots represent contact points. Minor axis ticks in millimetres [*mm*].

contact points a liquid pocket forms. In these regions liquid holds onto the contact point due to surface tension force and wall adhesion effect. The liquid pockets assume an oval and constantly deforming shape and, often, a liquid tail forms connecting the pocket to the following one creating a water bridge responsible for liquid flow. Only for very high gas flow rates some regions partially dry out. An example of fully developed film flow is reported in Fig. 9.

4.1.3. Transition flows

The transition between bubbly and film flow is not abrupt but occurs passing trough some intermediate patterns. Starting from a bubbly flow and increasing the gas flow rate the plate's cross section is filled by bubbles that tend to coalesce. This causes the formation of bubbles that exceed the corrugation dimension but still coexist with the fine or coarse bubbles depending on the breakage phenomenon strength. Since these bubbles are larger than the corrugation, they extend on more than one of them and assume an irregular zigzagged shape (Fig. 10a). Buscher (2019) defined these structures Taylor-like bubbles because as Taylor bubbles in tubes' slug flow their formation is due to coalescence and their dimension is constrained by the geometry of the plate. Increasing the gas flow rate even more, Taylor-like bubbles become more frequent. They become wider and different Taylor-like bubbles come in contact entrapping liquid regions. If the gas patches are distinguishable and surrounded by gas bubbles, an heterogeneous flow pattern is established. Increasing the gas flow rate furthermore, the entrapped liquid is limited to contact points and the gas patches are the predominant flow structure in the corrugated plate but they are not so stable to form a full film flow. This is referred to as partial film flow. This is transition between regimes is continuous, and, increasing the gas flow rate even more, a stable film flow could be observed. Examples of these transition flow patterns are reported in Fig. 10.

The Taylor-like bubbles are seen to coexist with smaller bubbles of about the same size of the ones observed for the purely bubbly flow observed at the same liquid flow rate as shown in Fig. 11. In this regime the Taylor bubbles are flat and extend around the contact points but can not fully surround them. Taylor bubbles flow straight upward but its branches extend and contract in order to follow the wavy longitudinal path.

Heterogeneous flow is characterized by the merging of Taylor bubbles that form gas patches. This regime exhibits slightly different behavior at high and low flow rates. At low flow rates the pathces tend to assume the shape of a stream of Taylor-like bubbles keeping its ramified structure while, on the contrary, at high flow rates it resembles more

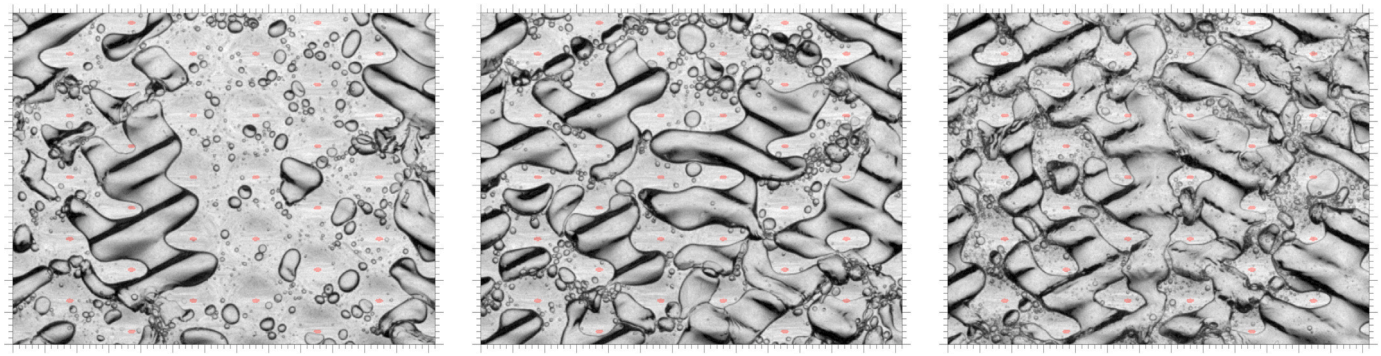

(a) (b) (c)

Fig. 10. Example of transition flow pattern: (a) Taylor-like, (b) Heterogeneous flow and (c) Partial film flow. Pictures from experiments. Red dots represent contact points. Minor axis ticks in millimetres [*mm*].

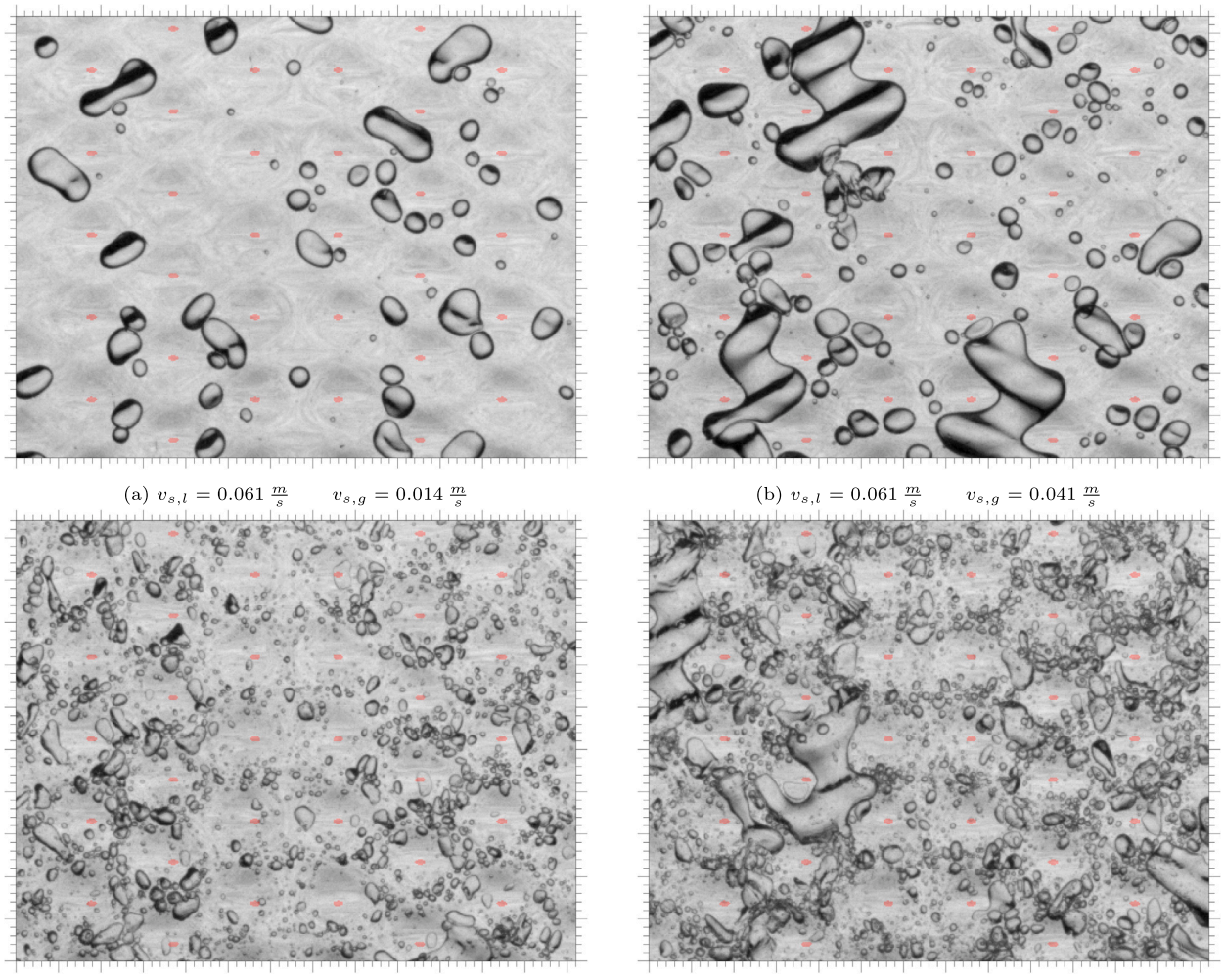

(a) $v_{s,l} = 0.061\ \frac{m}{s}$ $v_{s,g} = 0.014\ \frac{m}{s}$ (b) $v_{s,l} = 0.061\ \frac{m}{s}$ $v_{s,g} = 0.041\ \frac{m}{s}$

(c) $v_{s,l} = 0.366\ \frac{m}{s}$ $v_{s,g} = 0.069\ \frac{m}{s}$ (d) $v_{s,l} = 0.366\ \frac{m}{s}$ $v_{s,g} = 0.182\ \frac{m}{s}$

Fig. 11. Pure bubbly flow and Taylor-like bubbly flow at low liquid mass flux (a, b) and high liquid mass flux (c, d). Red dots represent contact points. Minor axis ticks in millimetres [*mm*].

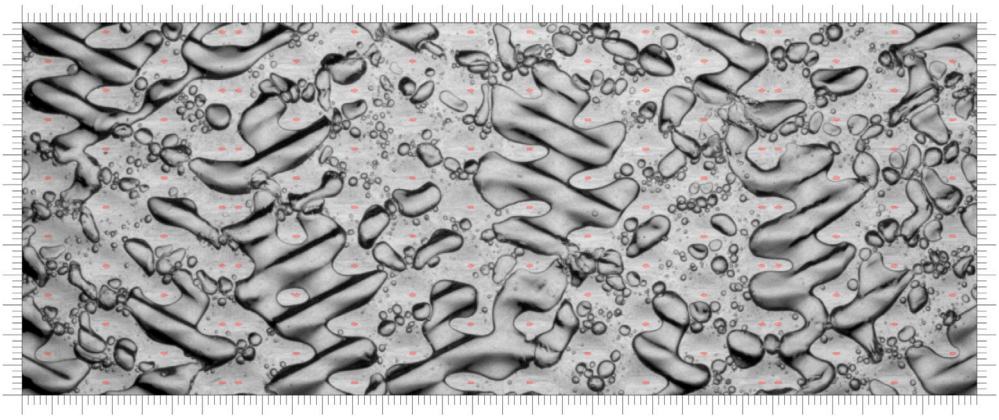

$Q_{s,l} = 0.061\ \frac{m}{s}$ $Q_{s,g} = 0.211\ \frac{m}{s}$

(a) Low liquid flow rate heterogeneous flow

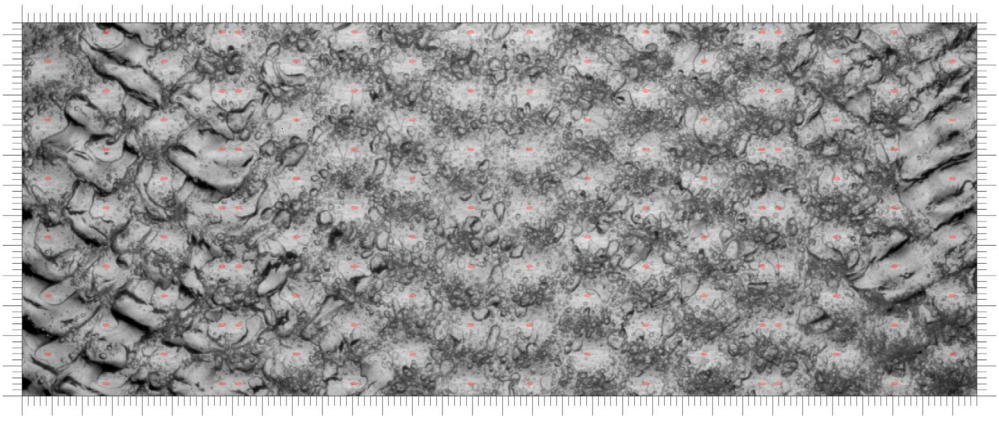

(b) $Q_{s,l} = 0.061\ \frac{m}{s}$ $Q_{s,g} = 0.211\ \frac{m}{s}$

(c) High liquid flow rate heterogeneous flow. Red dots represent contact points. Minor axes ticks in millimetres $[mm]$.

Fig. 12. Examples of heterogeneous flow at different flow rates. Pictures from experiments. Red dots represent contact points. Minor axis ticks in millimetres [*mm*].

a large gas cluster as can be observed in Fig. 12. In both cases regions characterized by bubbly flow are still present.

Partial film flow necessitates complete gas patch coverage across the entire section, with only isolated liquid regions allowed. The presence of these liquid regions can disrupt the integrity of the liquid patches at the contact points, often flushing them away and continuously reforming.

4.1.4. Intermittent flows

When both the liquid and gas superficial velocity are very high, intermittent gushes originating from the premixer are observed. In the region in which such phenomenon occurs, it would be expected a film or partial film flow. Actually the observed flow pattern maintain some characteristics of such flows, but continuous disturbance are evident. These gushes can cause liquid pockets to be pulled away from the plate, which then take time to reform. The higher is the liquid flow rate the more frequent the gushes become and it becomes difficult to distinguish the instabilities due to the gushes from a still not stable partial film. For this reason such conditions were labeled as Unstable Flow, but should be taken in account that this effect has to be attributed to the geometry of the flow distribution plenum. In Fig. 13 is shown the instant in which a gush passes through the channel forming a disturbance wave parallel to the corrugation direction.

4.2. Flow patterns map

The results of the visualization campaign performed are summarized on a superficial velocity map presented in Fig. 14. A total of 263 points have been investigated, recorded and carefully visualized to assess the flow pattern.

At constant liquid superficial velocity, it can be observed that the flow evolves from Bubbly to Film Flow passing trough Taylor-like Bubbly Flow, Heterogeneous Flow and Partial Film Flow. The liquid superficial velocity has an impact on bubble dimension. The bubbly flow is observed to be coarse for low liquid velocity and fine for high liquid velocities. Moreover, for higher liquid velocities the transitions are observed to occur at higher gas velocity too. Only a few points were characterized by instabilities strong enough not to allow to distinguish between partial and developed film flow.

5. Discussion and comparison

As highlighted in Section 1.1, this paper aim not only at improving the knowledge by investigating a very broad range of operating conditions but it also focuses on obtaining general criteria for transition lines in order to set a basis for future works. In order to do so, our own observations have been compared to other studies and to do so it was necessary to recognize and categorize the other studies results according to our nomenclature. After the re-categorization process, aggregated flow regime maps are displayed and new general correlations for transition prediction proposed.

5.1. Flow patterns re-categorization

In this part of the paper, the flow patterns observed in the different studies are re-categorized using the nomenclature presented in this

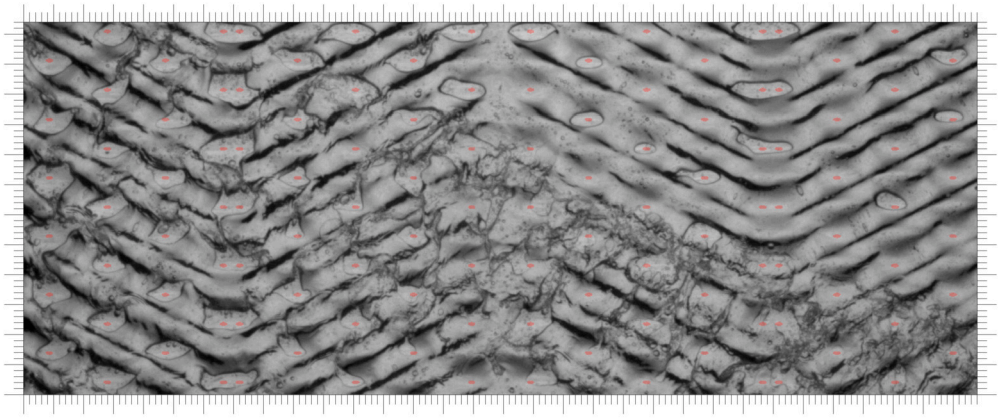

Fig. 13. Example of unstable flow. Picture from experiments. Red dots represent contact points. Minor axis ticks in millimetres [*mm*].

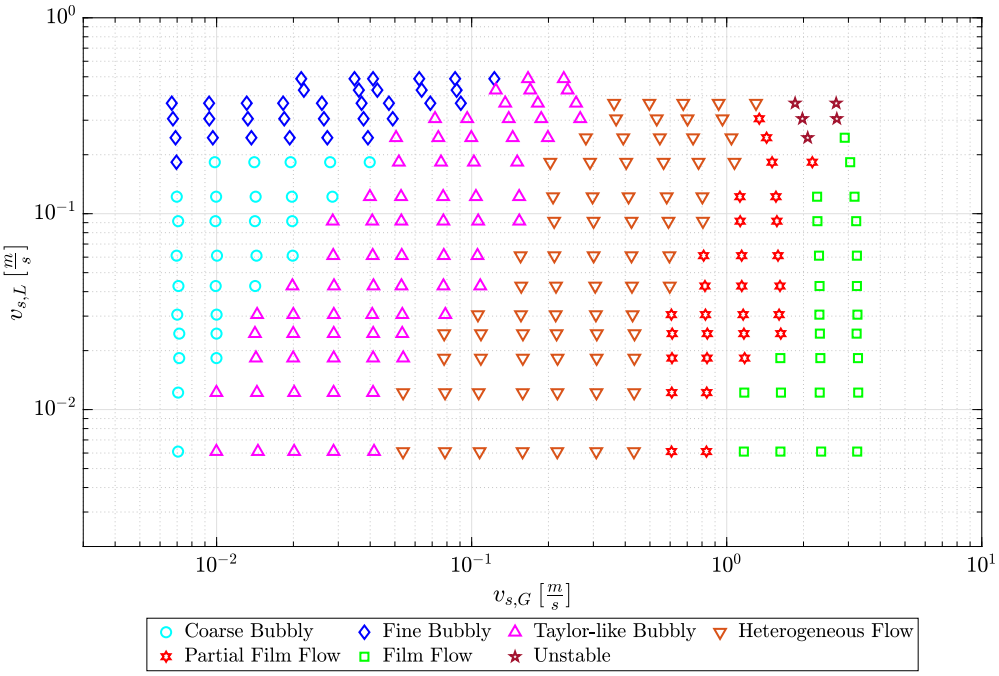

Fig. 14. Flow regime map from data produced in the present study.

work. The authors have gone through all the visualization database provided by the aforementioned experimental studies and checked which definition corresponded with the one given in this work. In this way, it was possible to group all the visualization data into a single database. Flow pattern are then divided into discrete categories according to the same flow characteristics. A visual comparison between studies results is proposed in order to justify the flow pattern attribution.

5.1.1. *Bubbly flows*

The bubbly flow patterns were divided into fine and coarse ones but most of the considered studies reported only one of the two patterns. The Fine Bubbly Flow was named by Buscher (2019) regular bubbly flow. Tribbe and Müller-Steinhagen (2001b) observed a regular bubbly flow characterized by bubble breakage and hence its expected to be fine bubbly flow. Vlasogiannis's (2002) B flow pattern was recognized to be a bubbly flow but the single bubbles could not be observed because his experimental set up could not catch small gas structures, for this reason it is expected that the B pattern was related to a fine bubbly flow. Grabenstein et al. (2017) used same classification of Tribbe and Müller-Steinhagen (2001b) so also Grabenstein et al. (2017) most probably observed fine bubbly flow. In Fig. 15 visual observation of different studies Fine Bubbly Flows are proposed.

The Coarse Bubbly Flow in Buscher (2019) was referred to as "irregular bubbly flow". Nilpueng and Wongwises (2010) and Shiomi et al. (2004) both presented images of coarse bubbly flow but they did not classified it differently from fine bubbly flow. In Fig. 16, visual observation of different studies Coarse Bubbly Flows are proposed.

5.1.2. *Film flow*

The Film Flow definition is used by Tribbe and Müller-Steinhagen (2001b), by Buscher (2019) and by Grabenstein et al. (2017). The Partial Film observed by Tribbe and Müller-Steinhagen (2001b) is still considered film flow in present work, because they defined it partial due to the local drainage of contact points and not due to the underdevelopment of the film. The Vlasogiannis's (2002) "A" flow pattern and Nilpueng's (2010) Annular-liquid Bridge Flow descriptions correspond to Film Flow. The visual observations of film flow in different studies are displayed in Fig. 17.

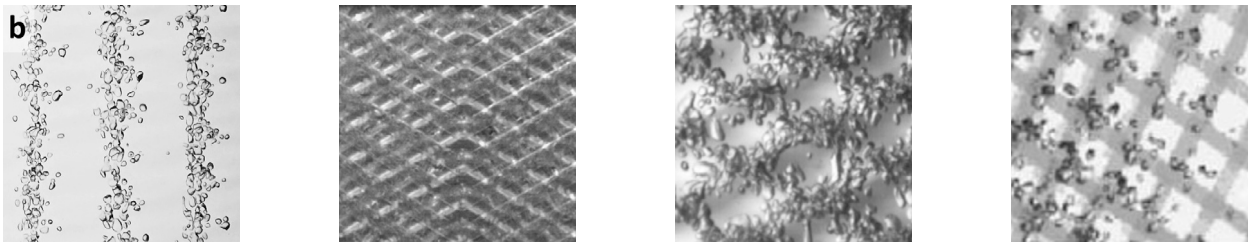

Fig. 15. Fine bubbly flow pattern observed in different studies: (a) Buscher (2019), (b) Vlasogiannis et al. (2002), (c) Grabenstein et al. (2017), (d) Shiomi et al. (2004).

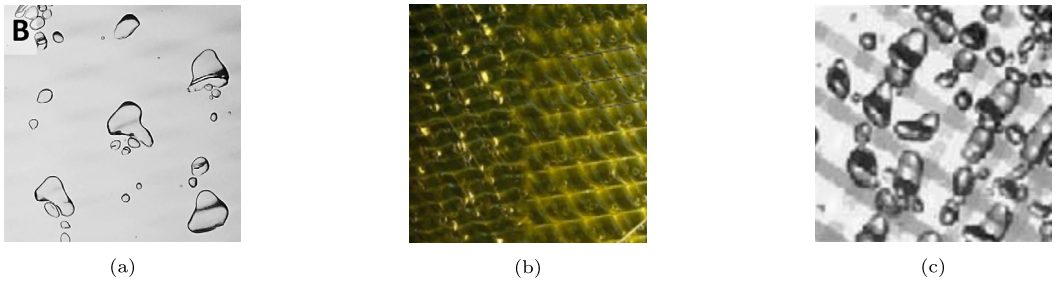

Fig. 16. Coarse bubbly flows observed in different studies: (a) Buscher (2019), (b) Nilpueng and Wongwises (2010) and (c) Shiomi et al. (2004).

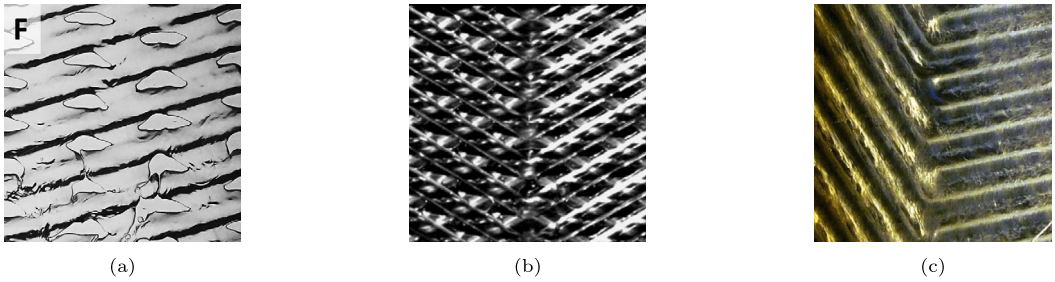

Fig. 17. Film flow observed in different studies: (a) Buscher (2019), (b) Vlasogiannis et al. (2002), (c) Nilpueng and Wongwises (2010).

5.1.3. Transition flows

The Transition Flows observed by Buscher (2019) are Taylor-like Bubbly Flow, Heterogeneous Flow and Partial Film Flow. Tribbe and Müller-Steinhagen (2001b) observed the phenomenon of Taylor-like bubbles and defined that pattern irregular bubbly flow, same nomenclature was used by Grabenstein et al. (2017). Vlasogiannis et al. (2002) observed Taylor-like bubbles in the "BA" flow pattern and late transition with Taylor bubbles interacting with each other was observed in "AB" flow pattern. All the different types of Transition Flows are reported in Fig. 18.

5.1.4. Intermittent flows

In present work the intermittent flow was attributed to instabilities in the plenum. Tribbe and Müller-Steinhagen (2001b) referred to intermittent flows as Churn Flow, Vlasogiannis's (2002) "C" Flow Pattern corresponded to Slug Flow, Grabenstein et al. (2017) distinguished between Slug and Churn Flows, Nilpueng and Wongwises (2010) visualized Slug Flow in the downward configuration. In Fig. 19 visualizations of Slug Flow by the different studies are reported. The legitimacy of considering Intermittent Flows as a flow pattern is a subject to debate. Buscher (2019) attributed the formation of intermittent flows to the distribution system and to pressure oscillation upstream the visualization section and stated that they can be completely avoided with a meticulous design. Vlasogiannis et al. (2002) observed that slug at the portholes influenced the slug in the plate but this was not a sufficient condition for its presence. Nilpueng and Wongwises (2010) observed it in downward flow but not in the upward for the same flow rates. Grabenstein et al. (2017), on the other hand, observed intermittent flows even with a specially designed mixer for avoiding slug at inlet and declared that instabilities were not artificially created. Present authors' results do not completely clarify the question but since the intermittency was observed to be generated from the plenum without a developing region the given interpretation is that it is an effect not generated by the plate itself but by external causes.

5.1.5. Other flow patterns

Besides the flow pattern highlighted till now, other different and non-conventional patterns were observed in the considered studies. These are the "Stagnant" flow observed by Buscher (2019), the "Separated flow" observed by Shiomi et al. (2004), the "Annular-liquid Bridge/Air Only Flow" observed by Nilpueng and Wongwises (2010) and the "Bubble Recirculation Flow" observed by the same authors. This last pattern is located in between the bubbly and the film flow and shows two patterns flowing in parallel, for this reason it could be considered a particular transition occurring in asymmetrical mixed geometries. In Fig. 20 examples of these other regimes could be visualized.

5.2. Data-synthesis on flow regimes map

As already highlighted, some of the studies are not strictly comparable because of different setups and operating conditions. The experimental campaign of Nilpueng and Wongwises (2010), for example,

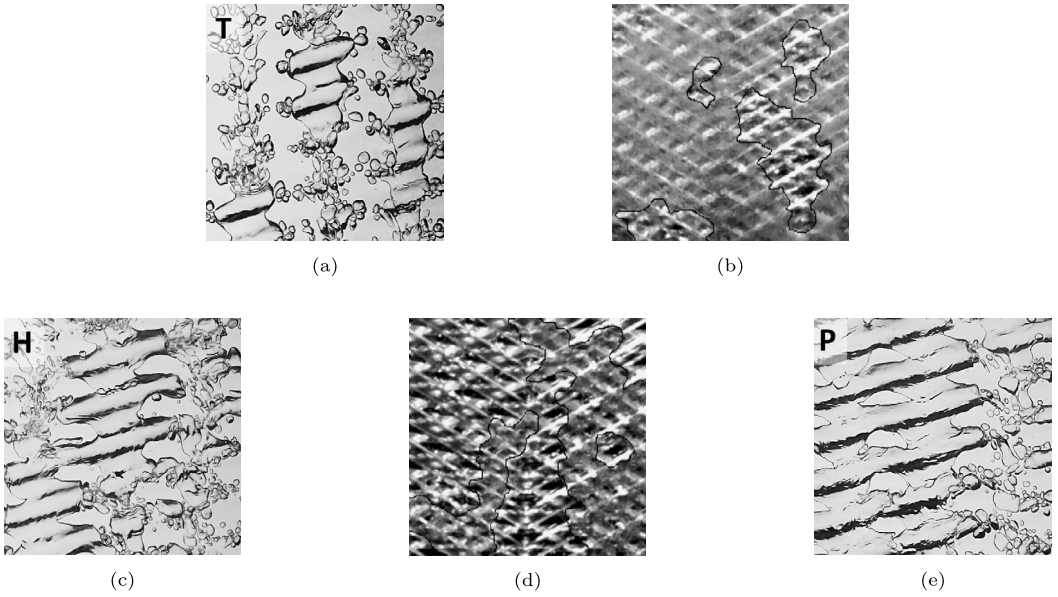

Fig. 18. Transition flow observed in different studies: (a) Taylor-Like Bubbly Flow by Buscher (2019), (b) "BA" flow pattern by Vlasogiannis et al. (2002), (c) Heterogeneous Flow by Buscher (2019), (d) "AB" Flow by Vlasogiannis et al. (2002), (e) Partial Film Flow by Buscher (2019).

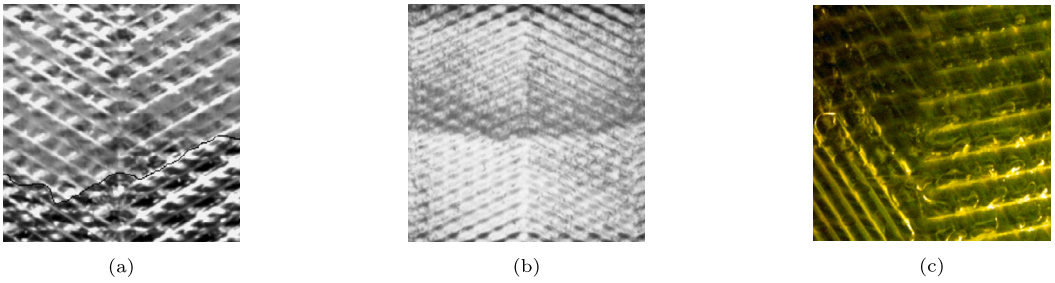

Fig. 19. Slug Flows observed in different studies: (a) Vlasogiannis et al. (2002), (b) Grabenstein et al. (2017) and (c) Nilpueng and Wongwises (2010).

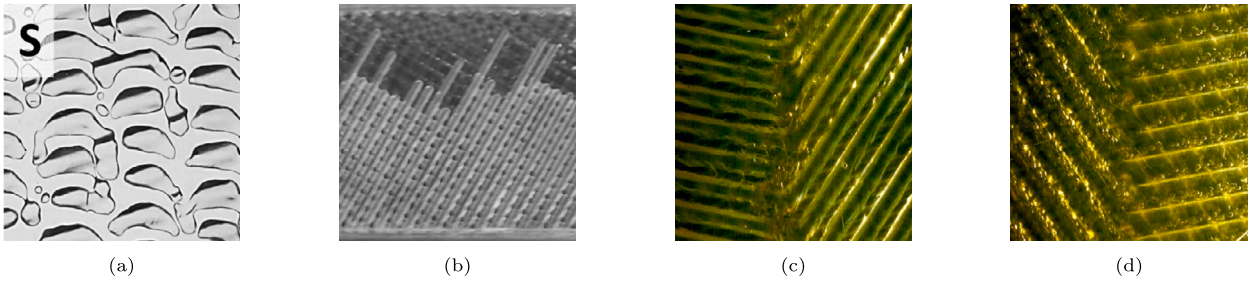

Fig. 20. (a) Stagnant Flow by Buscher (2019), (b) Separated Flow by Shiomi et al. (2004), (c) Annular-liquid Bridge/Air only Flow by Nilpueng and Wongwises (2010) and (d) Bubble Recirculation Flow by Nilpueng and Wongwises (2010).

was excluded from the comparison because of the unsymmetrical geometry used which could cause the flow patterns to be significantly different from the ones observed in other studies. Instead, the work of Shiomi et al. (2004) was not considered because of the high maldistribution observed that made it hardly comparable. The remaining studies were compared on a superficial velocity basis. Grabenstein et al. (2017) momentum flux maps were converted using the properties of fluids at reference conditions. Moreover, since most of the studies did not specify whether the provided maps were based on actual or reference conditions, in this work the flow regime maps were plotted keeping the same conditions of the relative study. This introduces a mismatch in the results but it has to be taken in account that most of studies were operated with the outlet of the test section at almost atmospheric pressure and hence the difference between actual and reference conditions is determined only by pressure drops that are usually relatively small compared to the operating pressure. A conversion from actual to reference conditions would not be possible because the pressure and temperature condition at each point is not reported in any of the studies. Additionally should be taken in account that different geometries and flow directions have been compared together because, although such parameters have an effect on flow transition, the effect is not so significant to alter the underlying mechanism. Buscher (2019) observed indeed minimal differences between flow pattern transitions in upward, downward and horizontal flows and Tribbe and Müller-Steinhagen (2001b) observed that the Chevron-angle mainly impacted only on intermittent flows.

In Fig. 21 the domains of the considered experimental studies are reported. It can observed that the region in which all the studies over-

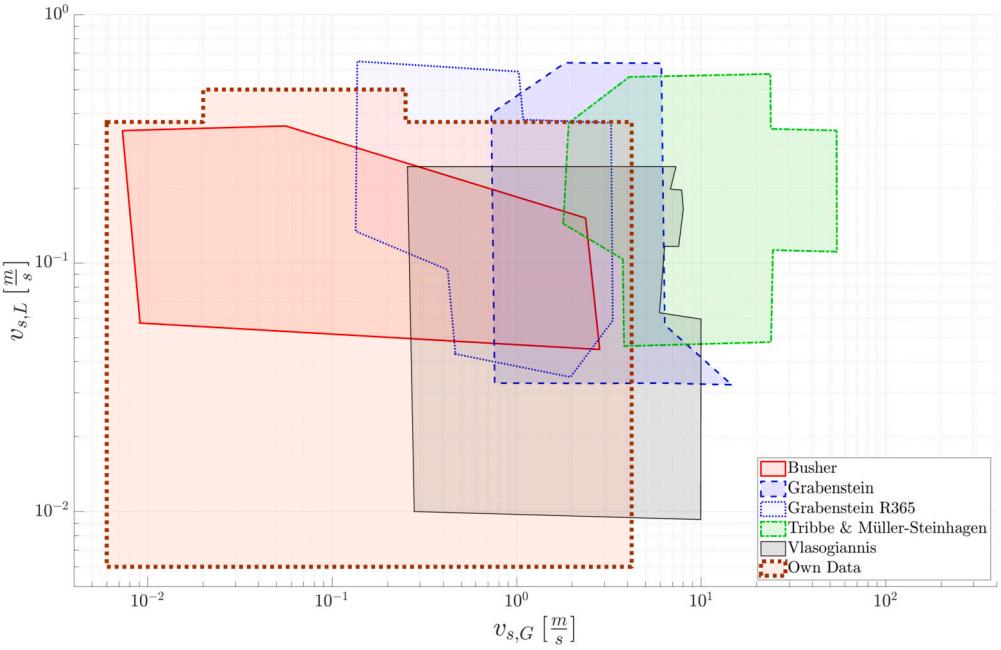

Fig. 21. Domains of the experimental studies considered in this work for flow regime maps comparison.

lap is very small. Buscher (2019) was the only author whose data cover the region with small gas superficial velocity. Vlasogiannis et al. (2002) instead were the only ones to cover the region with small liquid superficial velocity. Tribbe and Müller-Steinhagen (2001b) focused mainly on the region at high gas superficial velocity. Grabenstein et al. (2017) data instead are the most centered with respect the other studies and have a good overlapping with all other studies. In addition, when considering the R365mfc working fluid, its testing domain is shifted to lower gas superficial velocities. The present study's database allows to cover both the low water and low air regions, overlapping to Buscher's (2019) and Vlasogiannis's (2002) data and also investigating the low liquid region which is yet to be studied in literature.

In Fig. 22 all the experimental points from the different datasets are reported on the same map. All points are plotted independently on flow direction, plates geometry and operating fluid. This could cause mismatching but Buscher (2019) stated that the impact of flow direction on flow patterns is negligible for high Froude numbers. Moreover, no distinction is made on this map regarding the three different transition flows identified in subsection 5.1.3 as no clear re-classification was possible due to the lack of information reported in the analyzed papers. Therefore, transition flow regimes are treated as a whole category even when considering the data obtained from the experimental campaign reported in this study for better comparability with the other databases. Tribbe and Müller-Steinhagen (2001b) observed that the plates geometry mainly impacted on slug flow that, as described in previous sections, seems to be strictly related to the inlet of the two-phase mixture. The impact of different fluids can be observed only in the data from Grabenstein et al. (2017) and some considerations will be made in next section.

The obtained global flow regime map allows for some considerations. First of all, the intermittent flow regions observed in the different studies are clearly mismatched one from the other with only few points superimposed. The common aspect is that those regions are characterized by both high liquid and gas flow rates. For this reason Buscher's (2019) statement about slug flow in PHEs being caused only by inlet and outlet regions seems correct and so, in the present work, slug flow will be considered as a separated effect when discussing transition between flow patterns. Therefore, to predict intermittent flow, it is necessary to investigate the premixing or distribution section of the channel in detail. In the present work, a comprehensive analysis of the channel inlet has not been carried out, so it is only possible to state that intermittent flow occurs at high liquid and gas surface velocities, without the development of quantitative criteria. The second consideration is that where Grabenstein et al. (2017) and Vlasogiannis et al. (2002) observed the fine bubbly flow, Buscher (2019) and present authors observed transition flow. This can not be totally attributed to the use of actual conditions instead of reference one when representing the data points on the map because the error introduced would not be enough to cover the mismatch. It is instead very likely that while Buscher (2019) and present authors considers the transition flow as the first Taylor-like bubbles appear in the visualization window, the other two studies may refer to it as the Taylor-like structures become the prevalent pattern therefore moving the transition towards higher gas superficial velocities. The third consideration is that there is a mismatch also in the region where Tribbe and Müller-Steinhagen (2001b) and Vlasogiannis et al. (2002) observe transition flow, while Buscher (2019) and Grabenstein et al. (2017) observe film flow. By looking at our data, both film flow and transition can be observed in correspondence of the same velocity range. Also in this case, it is expected that this mismatch is due to the subjectivity in defining the transition to film flow. In conclusion, we can state that the mismatch between the different databases is not only due to the slightly different chevron geometry parameters, such as corrugation angles, depth, and wavelength. Other factors, such as the operating conditions, the calculation of superficial velocities, the definition and identification of flow regimes, and the recognition of the fully developed regime, also have a significant impact on the outcomes. We attempted to minimize these factors by uniforming our database to reference conditions where possible, and by analyzing the flow images and definitions provided by the different authors. However, we acknowledge that there is still some degree of subjectivity and uncertainty involved in these processes. Therefore, we suggest that the differences in results are better explained by a combination of these factors rather than by chevron geometry alone.

5.3. Semi-theoretical transition lines

In order to better identify the flow patterns and find a physically-sound method to recognize them, some transition criteria could be considered and hence some transition lines were defined. The theory exposed in Buscher (2019) is adapted and extended in to be more general

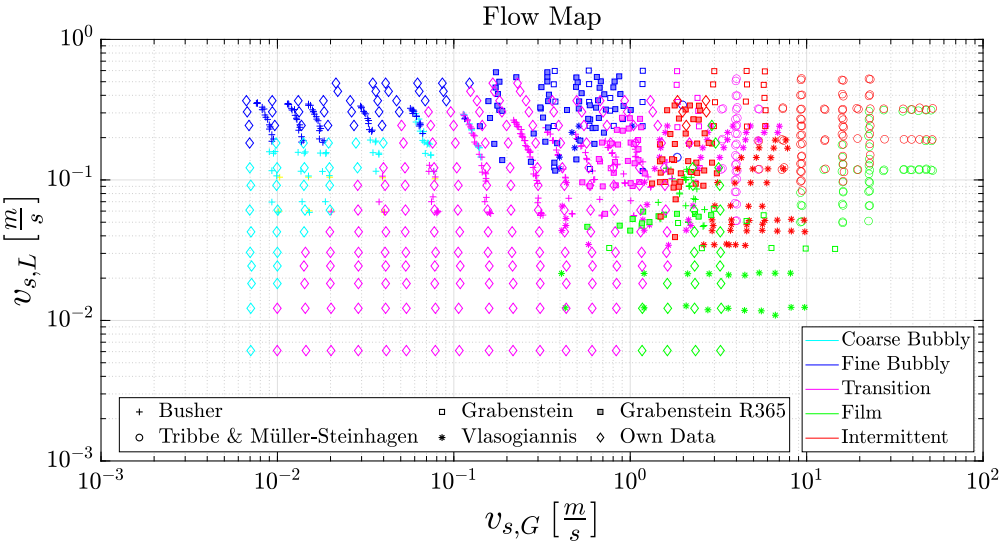

Fig. 22. Comprehensive flow regime maps that synthetizes the most relevant datasets present in literature as well as original data from the present work.

and to fit not only her experimental database but all the experimental studies.

The first transition line to be taken in account is the one from bubbly flow to transition flow. This is characterized by the formation of Taylor-like bubbles. For this reason the main transition mechanisms must be similar to the Taylor bubbles formation in pipes. Taitel et al. (1980) recognized bubble coalescence in absence of breakage to occur for statistical reason when the bubbles are packed with less than one half diameter distance, corresponding to a void fraction of 0.25. Breakage causes delay in coalescence until the maximum packing for round bubbles is reached, value that corresponding to a void fraction of 0.52. Buscher (2019) approximated the flow as homogeneous and considered void fraction between 0.25 and 0.52 a zone of coexistence of roundish and Taylor-like bubbles. In the present paper a little modification is applied to better represent the experimental data. The general idea is that the geometry of the plates and in particular the contact points have a role in delaying Taylor-like bubbles by impeding them to accelerate. For this reason, the limit assumed for coarse bubbly flow is a void fraction of 0.4 which, under the assumption of homogeneous flow) corresponds to the volumetric quality. When bubble breakage occurs, the formation of coalesced bubbles is of course delayed and therefore this limit is moved to 0.8 to fit the experimental data. This threshold allows the inclusion of fine bubbly data from Vlasogiannis et al. (2002) and Grabenstein et al. (2017) in the fine bubbly flow regime area in the flow map. This is apparently non-physical because when the bubbles reach the theoretical maximum packing value, the void fraction would be 0.52 which is considerably lower than the value previously proposed. But it should not be neglected that homogeneous flow model could be very different from reality in these operating conditions and so the threshold values expressed as volumetric fraction would be different from the void fraction limits posed by Taitel. A model is necessary to accurately compute the void fraction from the volumetric quality in a corrugated channel but no correlations for PHEs have ever been developed. Considering slip between gas and liquid phases, the void fraction would be certainly lower than the volumetric quality explaining the difference between the experimental and the theoretical value. These two transition lines are indicated as a and c in Fig. 23 and are expressed using the following equations where α is void fraction, x_V is volumetric quality, s is slip ratio, $v_{s,L}$ and $v_{s,G}$ the superficial liquid and gas velocities:

$$\alpha = x_V \quad s = 1 \quad homogeneous\ flow \tag{19}$$

$$v_{s,L} = \frac{1 - x_v}{x_v\, v_{s,G}} \quad or \quad v_{s,L} = \frac{1 - \alpha}{s\,\alpha\, v_{s,G}} \tag{20}$$

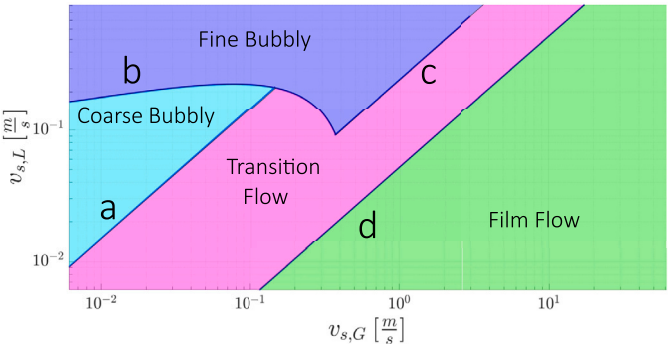

Fig. 23. Semi-Theoretical Transition lines.

A criterion for transition between fine and coarse bubbly flow is then fundamental to distinguish the two patterns. Hinze (1955) studied turbulent emulsification of a liquid into another assuming that the order of magnitude of the forces associated to surface tension had to be of the same order of the ones associated to turbulent kinetic energy and expressing the latter as function of energy dissipation rate (ϵ) and surface tension (σ). He obtained the following equation for maximum drop diameter:

$$d_{max} = k \left(\frac{\sigma}{\rho_l}\right)^{\frac{3}{5}} \epsilon^{-\frac{2}{5}} \qquad k = 0.725 \tag{21}$$

Taitel et al. (1980) applied Hinze's (1955) results to gas-liquid systems modeling breakage in tubes and Barnea et al. (1982) improved it by changing the k constant as function of void fraction using Calderbank's formulation:

$$k = 0.725 + 4.15\,\alpha^{0.5} \tag{22}$$

Buscher (2019) adapted the theory to PHEs by assuming initially the maximum possible bubbles' diameter for a fine flow regime to be equal to the corrugation depth and the following Blasius type correlation for Darcy friction factor (eq. (23)) from her experimental work in order to express the energy dissipation rate according to Taitel et al. (1980) (eq. (24)):

$$f_d = A \left(\frac{v_{2ph}\, D_h}{\nu_l}\right)^n \qquad A = 19.9 \qquad n = -0.225 \tag{23}$$

Table 6
Prediction accuracy of transition model from fine to coarse bubbly flow (experimental data from Buscher (2019)).

	Database	Buscher			Own Data	All Data
		Downward	Upward	Horizontal		
Fine Bubbly	No. data points	25	21	27	34	107
	Prediction accuracy	92%	95%	89%	100%	94%
Coarse Bubbly	No. data points	15	21	15	29	80
	Prediction accuracy	60%	76%	87%	97%	83%

$$\epsilon = \frac{1}{2} f_d \frac{v_{2ph}^3}{D_h} \tag{24}$$

The author then obtained the best fit using a bubble diameter (D_h) slightly larger than corrugation depth.

In the present study a similar approach is used. It is assumed that the fine bubbles could have a diameter larger than the corrugation depth but always smaller than its double which corresponds to the maximum channel depth (eq. (25)). To consider this, a multiplier M between $\Phi/2$ and Φ (where Φ is the plate's enlargement factor) is introduced to express maximum bubble diameter as function of the channel hydraulic diameter. In terms of equations, these concepts can be expressed as:

$$b_p < D_{bub,max} < 2b_p \tag{25}$$

$$D_h = \frac{2b_p}{\Phi} \tag{26}$$

$$M = D_{bub,max}/D_h \quad \text{with} \quad 0.5\Phi < M < \Phi \tag{27}$$

Inserting equations (24) and (23) in equation (21) the mixture velocity can be expressed as:

$$v_{2ph} = \left(\frac{k\Phi}{2b_p M}\right)^{\frac{5}{6+2n}} \left(\frac{\sigma}{\rho_l}\right)^{\frac{3}{6+2n}} \left(\frac{A}{2}\right)^{-\frac{2}{6+2n}} \left(\frac{\rho_l}{\mu_l}\right)^{-\frac{2n}{6+2n}} \left(\frac{2b_p}{\Phi}\right)^{\frac{2-2n}{6+2n}} \tag{28}$$

and therefore relation between gas and liquid superficial velocities along the transition is expressed by:

$$v_{s,L} = v_{2ph} - v_{s,G} \tag{29}$$

The transition line was determined iteratively. For each superficial gas velocity a void fraction was assumed and used to compute mixture velocity, the volume quality was then computed and assumed equal to the void fraction (homogeneous model) and used as new hypothesis proceeding until convergence. A satisfying fit was obtained with a value of 0.75 for the M multiplier. The M parameter fitting also carries a physical significance. Specifically, it serves as a non-dimensional representation of bubble size, distinguishing whether the flow pattern is primarily influenced by coalescence (resulting in Coarse Bubbly Flow) or by breakage (leading to Fine Bubbly Flow). Notably, as the hydraulic diameter is solely determined by corrugation depths and wavelengths, this ratio establishes a fixed relationship between the bubble dimension and the geometric parameters of the corrugations.

Table 6 shows how well the proposed transition line is able to distinguish between fine and coarse bubbly flow taking as references the data from Buscher's work (2019) and our own database. The accuracy is defined as the ratio of the number of observed points that fall inside the region described by the proposed transition lines over the total number of observation for a specific flow regime. The other studies analyzed in this work were not considered in the benchmark they do not clearly distinguish between fine and coarse bubbly flow. The homogeneous flow correlation for friction factor used can be adapted for different dataset by changing the constants. In Fig. 23 the transition line between coarse and fine bubbly is indicated with the letter b.

The transition to film was observed by Buscher (2019) to become stable when the film region occupy the 90% of the channel, that was calculated to correspond approximately to a void fraction of 0.95. The use of homogeneous flow model for computing the transition line is more critical for film flow since a slip between phases is expected. This model is used anyway though because of the lack of an appropriate void fraction correlation for PHEs. The film flow transition line is hence expressed by equation (20) and indicated in Fig. 23 as d. It has to be highlighted that transition lines defined only by void fraction like the film one are fluid-independent on a superficial velocity plot. A difference can be observed only in the transition between coarse and fine bubbly as they depend on fluid properties. This can be noticed in transition lines of water and R365mfc plotted in Fig. 24. Unfortunately, Grabenstein's analysis (2017) does not provide sufficient data to verify if the transition between fine and coarse bubbly for R365mfc actually obeys to the prediction.

Table 7 shows the percentage of the correct predictions for each flow pattern. The prediction can not satisfy all the databases because of, as previously described, the non exact direct comparability of the studies and the subjective aspects related to flow visualization. The global prediction is very good for bubbly flow and for film flow, while only 58% of the transition flow data are correctly predicted. The underestimation of own and Buscher's (2019) transition data is to correctly predict Vlasogiannis's (2002) and Grabenstein's (2017) bubbly regions and the underestimation of Vlasogiannis's (2002) and Tribbe's (2001b) transition region is to correctly predict Grabenstein's (2017), Buscher's (2019) and own film flow data. Tribbe's (2001b) bubbly flow is never correctly predicted, but the visualizations were just a few and performed starting from high gas superficial velocity if compared to other studies. This could have influenced the visualization of pure bubbly flow. Film flow transition line can accurately predict film flow observation across all studies. A big part of transition data from our own database enters the film region at low water superficial velocities. This may be due to the adoption of homogeneous flow model to describe void fraction. The authors expect a better representation of transitions with a real model for void fraction that accounts for slip between phases (especially important at low liquid flow rate and high gas one). The rest of own data prediction is perfectly in line with the comprehensive prediction of all experimental studies. In Fig. 25 the experimental data are reported together with the defined transition lines showing a good agreement.

A key issue for the analysis of two-phase flow in plate heat exchangers (PHEs) that should be addressed, is the applicability of adiabatic flow patterns to diabatic conditions. Studies focusing on flow visualization in two-phase Plate Heat Exchangers (PHEs) during evaporation and condensation are limited in number and typically consider the entire plate geometry including inlet and outlet distribution sections which could accentuate intermittencies due to instabilities and maldistribution. To address the applicability issue, we compared our results obtained from the analysis of adiabatic studies with the diabatic flow patterns reported by Lee et al. (2020, 2021) for boiling and condensation of R-1234ze(E) in a PHE. The authors visualized three different flow patterns which they named steady annular flow, pulsating annular flow and rough liquid film. From their definitions, we found that the steady annular and rough liquid film flows observed by Lee et al. are consistent with our film and transition flows, respectively, while the pulsating annular flow can go under the category of intermittent flow

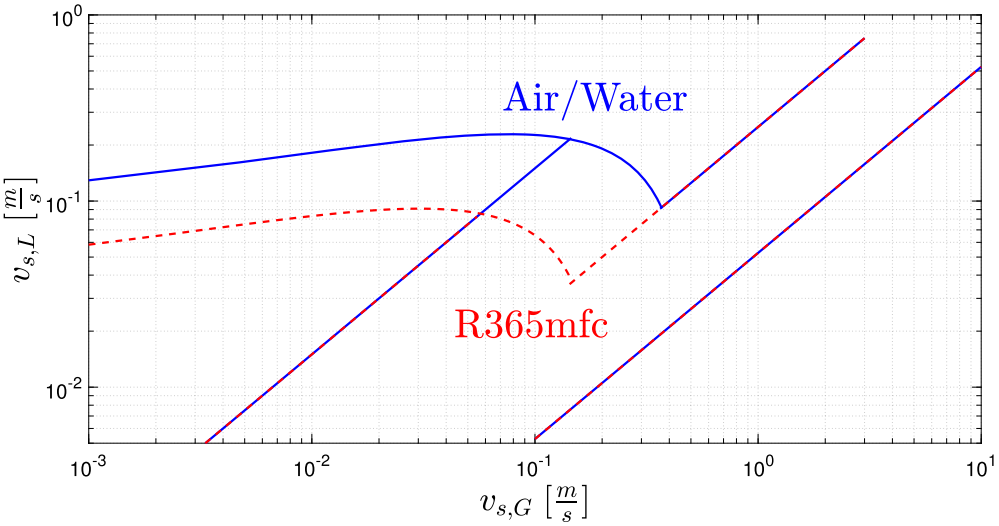

Fig. 24. Comparison between theoretical transition lines of water and R365mfc.

Table 7
Prediction accuracy of Transition Models compared with Experimental Studies.

	Database:	Buscher (2019)	Vlasogiannis et al. (2002)	Tribbe and Müller-Steinhagen (2001a)	Grabenstein et al. (2017)	Own Data	All Data
Bubbly	No. data points	124	7	4	79	63	277
	Prediction accuracy	96%	86%	0%	96%	98%	95%
Transition	No. data points	140	44	38	39	170	431
	Prediction accuracy	59%	50%	47%	82%	57%	58%
Film	No. data points	28	19	54	23	25	149
	Prediction accuracy	79%	95%	100%	91%	92%	93%

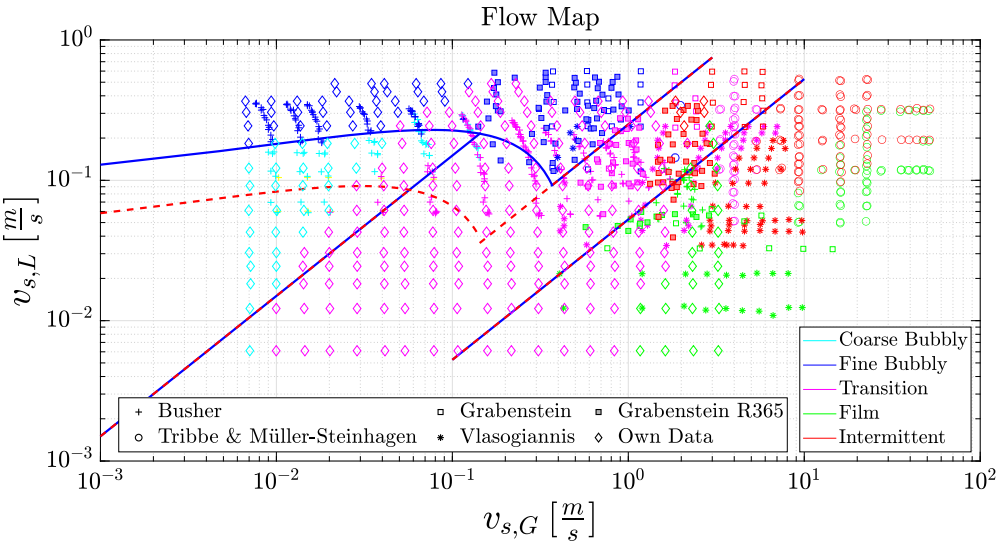

Fig. 25. Flow map of all experimental studies with semi-theoretical transition lines.

given the presence of strong intermittent disturbance waves as reported by the authors. The results of Lee et al. visualizations were converted in superficial velocities and compared with the flow map presented in our manuscript in Fig. 26. From this figure it can be noticed that the steady annular and rough liquid flows seem to be consistent with film and transition flows as observed in adiabatic conditions. On the other hand, the pulsating annular flow is close to the others study's intermittent region and, as an intermittent flow, it can not really be accurately predicted by the semi-theoretical lines proposed in this paper. Moreover, this flow pattern seems to occur at lower liquid superficial velocities than what observed in adiabatic facilities, maybe due to the asymmetrical inlet of commercial plates that favors flow instabilities.

The same considerations hold true in case of condensation. Lee et al. (2021) observed the disappearance of what they defined rough liquid film leaving only steady and pulsating annular flow as the predominant flow patterns. Fig. 27 shows the graphical comparison between the data analyzed in this study and the one proposed in Lee et al. (2021). Even in this case the transition between these two flow pattern seems to be

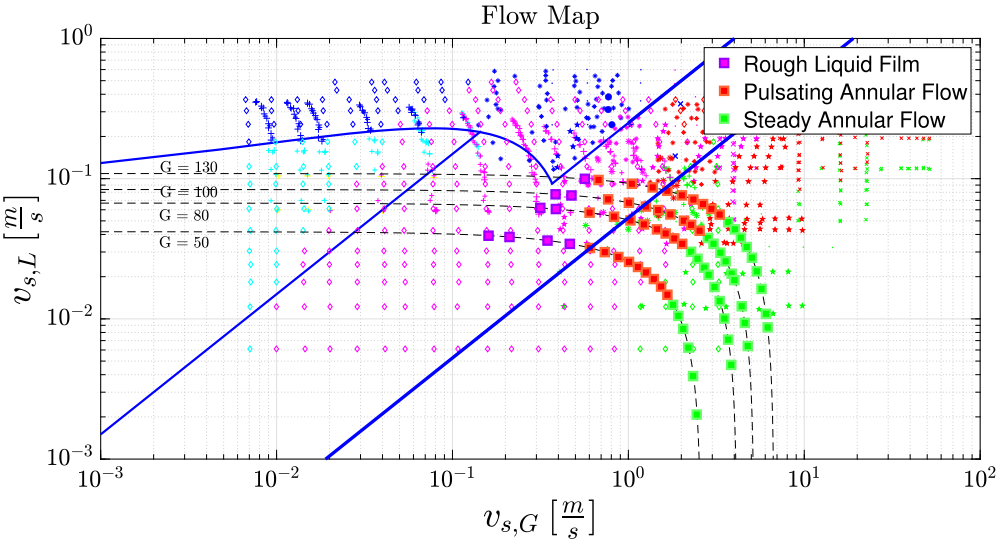

Fig. 26. Comparison with data points from Lee et al. (2020) regarding vertical flow boiling of R-1234ze(E).

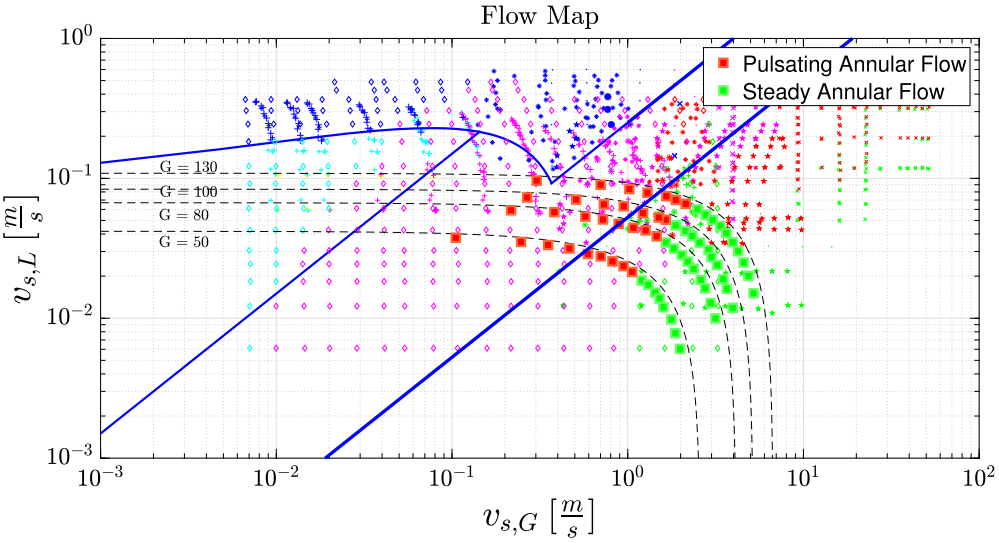

Fig. 27. Comparison with data points from Lee et al. (2021) regarding vertical condensation of R-1234ze(E).

consistent with what observed in adiabatic studies keeping in mind that the different flow direction (downward) may have an impact on flow instabilities.

Cheng et al. (2008) discussed instead the relationship between the physical mechanisms controlling two-phase flow and the flow patterns, emphasizing the importance of predicting flow patterns for heat transfer and pressure drops. They reviewed many studies on two-phase gas-liquid flow patterns and applicability of flow-pattern maps in adiabatic and diabatic conditions focusing on micro-scale channels. In this study it is pointed out that the diabatic flow maps should revert to adiabatic in case of heat flux approaching zero, and that adiabatic maps are commonly used for diabatic flow patterns prediction even if this should in principle be avoided. Also, the authors suggested that more research should be done to improve the understanding of the effects of heat transfer on flow patterns their transition mechanisms. Therefore, based on his review and our comparison with the diabatic flow patterns reported by Lee et al. (2020, 2021), we can conclude that the applicability of adiabatic flow patterns to diabatic conditions is not straightforward, and that it depends on several factors, such as the fluid properties, the channel geometry, the inlet conditions, the heat flux, and the flow direction. However, we also recognize that the study of adiabatic flow regimes is valuable, as it facilitates the exploration of phase interaction in the absence of heat transfer and provides a basis for the development of new correlations that can account for the additional effects introduced by heat flux.

6. Conclusions

The aim of this work was to highlight the most important parameters influencing the two-phase flow patterns in PHEs, to describe the flow regimes with a univocal definition and to compare different experimental databases to our experimental data in order to propose new and more general transition lines between the different patterns.

A new experimental facility for flow pattern visualization in a chevron-type corrugated plate was developed and high-framerate videos were acquired for visualization purposes. This allowed a precise definition of the visualized flow patterns with images reported as visual support. Furthermore, we found lack of common nomenclature for the definition of flow pattern in PHE. To address this issue, a new nomenclature was proposed in accordance with our own experimental

work and the data from the different studied were re-classified under the new naming convention.

The results of the flow visualization campaign were presented and discussed. A flow regime map casted in terms of gas and liquid superficial velocities was reported as main outcome of the experimental activity. The flow patterns and the observed transition mechanisms were thoroughly discussed and commented. A comprehensive data-synthesis from different studies was reported and all the experimental data from the various works were aggregated to display a more general flow map. The flow patterns observed in different studies are generally matching one another with some exceptions due to the intrinsic subjectivity of visual classification and the different configurations analyzed. Semi-Theoretical transition lines based on previous theoretical works were adapted and fitted to the database. These lines resulted adequate as a proxy for flow regime transitions with an average accuracy of the prediction of more than 80%.

Natural evolution of the analysis presented in this work would be the measurement of the actual void fraction in plate heat exchangers to define a model needed to drop the homogeneous flow assumption. This would be beneficial for a better definition of transition lines.

Nomenclature

α	Void Fraction
χ	Wave number
ϵ	Turbulent kinetic energy dissipation rate
Λ	Oshinowo's correction
λ	Corrugation Wavelength
Φ	Enlargement factor
ρ_l	Liquid Density
σ	Surface Tension
φ	Corrugation Angle
A_f	Frontal Area
B_p	Plate Width
b_p	Corrugation depth
D_h	Hydraulic Diameter
d_{max}	Maximum bubble/drop diameter
e_i	Uncertainty associated to the quantity i
f_d	Darcy friction factor
j_g	Dimensionless gas velocity
L_b	Corrugated section length
L_{tot}	Total plate length
M	Bubble maximum diameter Multiplier
P_{cal}	Pressure of the rotameter at which was calibrated
P_{man}	Pressure at rotameter
P_{PHE}	Operative Pressure of the PHE
P_{pl}	Pressure in the channel
P_{rot}	Rotameter Pressure
Q_i	Flow Rate of phase i
$Q_{read,g}$	Flow Rate reading at rotameter
Re_l	Liquid alone Reynolds number
s	Slip Ratio
T_{cal}	Temperature of the rotameter at which was calibrated
T_{pl}	Temperature in the channel
T_{rot}	Rotameter Temperature
v_{2ph}	Mixture Velocity
$v_{s,G}$	Gas Superficial Velocity
$v_{s,L}$	Liquid Superficial Velocity
x	Mass Quality
x_V	Volume Quality

CRediT authorship contribution statement

Stefano Passoni: Writing – review & editing, Writing – original draft, Visualization, Methodology, Investigation, Formal analysis, Data curation, Conceptualization. **Andrea Ferrario:** Writing – review & editing, Writing – original draft, Investigation, Formal analysis, Data curation. **Stefano Lorenzi:** Project administration, Funding acquisition, Conceptualization. **Riccardo Mereu:** Writing – review & editing, Supervision, Methodology, Conceptualization.

Declaration of competing interest

The authors declare the following financial interests/personal relationships which may be considered as potential competing interests: Stefano Passoni reports financial support and article publishing charges were provided by EU Framework Programme for Research and Innovation Euratom.

Data availability

Data will be made available on request.

Acknowledgements

This work has received funding from the Euratom research and training programme 2014-2018 under Grant Agreement No. 847553

References

Abu-Khader, M.M., 2012. Plate heat exchangers: recent advances. Renew. Sustain. Energy Rev. 16, 1883–1891. https://doi.org/10.1016/j.rser.2012.01.009.

Amalfi, R.L., Vakili-Farahani, F., Thome, J.R., 2016b. Flow boiling and frictional pressure gradients in plate heat exchangers. part 2: Comparison of literature methods to database and new prediction methods. Int. J. Refrig. 61, 185–203. https://doi.org/10.1016/j.ijrefrig.2015.07.009.

Amalfi, R.L., Vakili-Farahani, F., Thome, J.R., 2016a. Flow boiling and frictional pressure gradients in plate heat exchangers. part 1: Review and experimental database. Int. J. Refrig. 61, 166–184. https://doi.org/10.1016/j.ijrefrig.2015.07.010.

Asano, H., Takenaka, N., Fujii, T., 2004. Flow characteristics of gas-liquid two-phase flow in plate heat exchanger (visualization and void fraction measurement by neutron radiography). Exp. Therm. Fluid Sci. 28, 223–230. https://doi.org/10.1016/S0894-1777(03)00043-8.

Asano, H., Takenaka, N., Wakabayashi, T., Fujii, T., 2005. Visualization and void fraction distribution of downward gas–liquid two-phase flow in a plate heat exchanger by neutron radiography. Nucl. Instrum. Methods Phys. Res., Sect. A, Accel. Spectrom. Detect. Assoc. Equip. 542, 154–160. https://doi.org/10.1016/j.nima.2005.01.093.

Ayub, Z.H., 2003. Plate heat exchanger literature survey and new heat transfer and pressure drop correlations for refrigerant evaporators characterization of advanced heat exchanger performance of single and multi-phase flows view project. https://doir.org/10.1080/01457630390218074.

Ayub, Z.H., Khan, T.S., Salam, S., Nawaz, K., Ayub, A.H., Khan, M., 2019. Literature survey and a universal evaporation correlation for plate type heat exchangers. Int. J. Refrig. 99, 408–418. https://doi.org/10.1016/j.ijrefrig.2018.09.008.

Barnea, D., Shoham, O., Taitel, Y., 1982. Flow pattern transition for vertical downward two phase flow. Chem. Eng. Sci. 37, 741–744. https://doi.org/10.1016/0009-2509(82)85034-3.

Buscher, S., 2019. Visualization and modelling of flow pattern transitions in a cross-corrugated plate heat exchanger channel with uniform two-phase distribution. Int. J. Heat Mass Transf. 144, 118643. https://doi.org/10.1016/j.ijheatmasstransfer.2019.118643.

Buscher, S., 2021. Two-phase pressure drop and void fraction in a cross-corrugated plate heat exchanger channel: impact of flow direction and gas-liquid distribution. Exp. Therm. Fluid Sci. 126, 110380. https://doi.org/10.1016/j.expthermflusci.2021.110380.

Cheng, L., Ribatski, G., Thome, J.R., 2008. Two-phase flow patterns and flow-pattern maps: fundamentals and applications. Appl. Mech. Rev. 61, 050802. https://doi.org/10.1115/1.2955990.

Chisholm, D., 1967. A theoretical basis for the Lockhart-Martinelli correlation for two-phase flow. Int. J. Heat Mass Transf. 10, 1767–1778. https://doi.org/10.1016/0017-9310(67)90047-6.

Eldeeb, R., Aute, V., Radermacher, R., 2016. A survey of correlations for heat transfer and pressure drop for evaporation and condensation in plate heat exchangers. Int. J. Refrig. 65, 12–26. https://doi.org/10.1016/j.ijrefrig.2015.11.013.

Focke, W.W., Knibbe, P.G., 1986. Flow visualization in parallel-plate ducts with corrugated walls. J. Fluid Mech. 165, 73. https://doi.org/10.1017/S0022112086003002.

Grabenstein, V., Polzin, A.-E., Kabelac, S., 2017. Experimental investigation of the flow pattern, pressure drop and void fraction of two-phase flow in the corrugated gap of a plate heat exchanger. Int. J. Multiph. Flow 91, 155–169. https://doi.org/10.1016/j.ijmultiphaseflow.2017.01.012.

Gradeck, M., Lebouché, M., 2000. Two-phase gas–liquid flow in horizontal corrugated channels. Int. J. Multiph. Flow 26, 435–443. https://doi.org/10.1016/S0301-9322(99)00018-X.

Hinze, J.O., 1955. Fundamentals of the hydrodynamic mechanism of splitting in dispersion processes. AIChE J. 1, 289–295. https://doi.org/10.1002/aic.690010303.

JCGM, 2008. Evaluation of measurement data-guide to the expression of uncertainty in measurement Évaluation des données de mesure-guide pour l'expression de l'incertitude de mesure. http://www.bipm.org.

Jin, S., Hrnjak, P., 2017. A new method to simultaneously measure local heat transfer and visualize flow boiling in plate heat exchanger. Int. J. Heat Mass Transf. 113, 635–646. https://doi.org/10.1016/j.ijheatmasstransfer.2017.04.116.

Kang, J., Bak, J.Y., Lee, B.J., Chung, C.K., Yun, B., 2022. Numerical investigation of a plate-type steam generator for a small modular nuclear reactor. Nucl. Eng. Technol. 54, 3140–3153. https://doi.org/10.1016/j.net.2022.02.020.

Lee, D., Jo, C., Kim, B., Kim, Y., 2020. Boiling flow patterns and dry-out characteristics of r-1234ze (e) in a plate heat exchanger. Int. J. Heat Mass Transf. 161, 120308. https://doi.org/10.1016/j.ijheatmasstransfer.2020.120308.

Lee, D., Yun, S., Choi, J., Kim, Y., 2021. Flow patterns and heat transfer characteristics of r-1234ze (e) for downward condensation in a plate heat exchanger. Int. J. Heat Mass Transf. 175, 121373. https://doi.org/10.1016/j.ijheatmasstransfer.2021.121373.

Martin, H., 2010. N6 Pressure Drop and Heat Transfer in Plate Heat Exchangers. Springer Berlin Heidelberg, Berlin, Heidelberg, pp. 1515–1522.

Nilpueng, K., Wongwises, S., 2010. Two-phase gas-liquid flow characteristics inside a plate heat exchanger. Exp. Therm. Fluid Sci. 34, 1217–1229. https://doi.org/10.1016/j.expthermflusci.2010.05.001.

Shiomi, Y., Nakanishi, S., Uehara, T., 2004. Characteristics of two-phase flow in a channel formed by Chevron type plates. Exp. Therm. Fluid Sci. 28, 231–235. https://doi.org/10.1016/S0894-1777(03)00044-X.

Solotych, V., Lee, D., Kim, J., Amalfi, R.L., Thome, J.R., 2016. Boiling heat transfer and two-phase pressure drops within compact plate heat exchangers: experiments and flow visualizations. Int. J. Heat Mass Transf. 94, 239–253. https://doi.org/10.1016/j.ijheatmasstransfer.2015.11.037.

Taitel, Y., Barnea, D., Dukler, A.E., 1980. Modelling flow pattern transitions for steady upward gas-liquid flow in vertical tubes. AIChE J. 26, 345–354. https://doi.org/10.1002/aic.690260304.

Tao, X., Nuijten, M.P., Ferreira, C.A.I., 2018. Écoulement vertical descendant diphasique dans des échangeurs de chaleur à plaques: configurations d'écoulement et mécanismes de condensation. Int. J. Refrig. 85, 489–510. https://doi.org/10.1016/j.ijrefrig.2017.10.008.

Thulukkanam, K., 2000. Heat Exchanger Design Handbook. CRC Press.

Tribbe, C., Müller-Steinhagen, H.M., 2001a. Gas/liquid flow in plate-and-frame heat exchangers - part i: Pressure drop measurements. Heat Transf. Eng. 22, 5–11. https://doi.org/10.1080/01457630118144.

Tribbe, C., Müller-Steinhagen, H.M., 2001b. Gas/liquid flow in plate-and-frame heat exchangers - part ii: Two-phase multiplier and flow pattern analysis. Heat Transf. Eng. 22, 12–21. https://doi.org/10.1080/01457630150215686.

Vlasogiannis, P., Karagiannis, G., Argyropoulos, P., Bontozoglou, V., 2002. Air–water two-phase flow and heat transfer in a plate heat exchanger. Int. J. Multiph. Flow 28, 757–772. https://doi.org/10.1016/S0301-9322(02)00010-1.